Kinetoplastid-specific X2-family kinesins interact with a kinesin-like pleckstrin homology domain protein that localizes to the trypanosomal microtubule quartet

Corinna Benz[1], Nora Müller[2], Sabine Kaltenbrunner[1,2,†], Hana Váchová[3], Marie Vancová[1,2], Julius Lukeš[1,2], Vladimír Varga[3], Hassan Hashimi[1,2,*]

[1]Institute of Parasitology, Biology Center, Czech Academy of Sciences, České Budějovice, Czechia

[2] Faculty of Science, University of South Bohemia, České Budějovice, Czechia

[3]Laboratory of Cell Motility, Institute of Molecular Genetics of the Czech Academy of Sciences, Prague, Czechia

[†]Current address: Johannes Kepler University, Medical Faculty, Linz, Austria

*Corresponding author: hassan@paru.cas.cz

Running title: X2 kinesins interact with TbPH1 at microtubule quartet

ABSTRACT

Kinesins are motor proteins found in all eukaryotic lineages that move along microtubules to mediate cellular processes such as mitosis and intracellular transport. In trypanosomatids, the kinesin superfamily has undergone a prominent expansion, resulting in one of the most diverse kinesin repertoires that includes the two kinetoplastid-restricted families X1 and X2. Here, we characterize in *Trypanosoma brucei* TbKifX2A, an orphaned X2 kinesin. TbKifX2A tightly interacts with TbPH1, a kinesin-like protein with a likely inactive motor domain, a rarely reported occurrence. Both TbKifX2A and TbPH1 localize to the microtubule quartet (MtQ), a characteristic but poorly understood cytoskeletal structure that wraps around the flagellar pocket as it extends to the cell body anterior. The proximal proteome of TbPH1 revealed two other interacting proteins, the flagellar pocket protein FP45 and intriguingly another X2 kinesin, TbKifX2C. Simultaneous ablation of TbKifX2A/TbPH1 results in the depletion of FP45 and TbKifX2C and also an expansion of the flagellar pocket, among other morphological defects. TbKifX2A is the first motor protein to be localized to the MtQ. The observation that TbKifX2C also associates with the MtQ suggests that the X2 kinesin family may have co-evolved with the MtQ, both kinetoplastid-specific traits.

Keywords: Trypanosoma, kinesin, cytoskeleton, microtubules, microtubule quartet, morphogenesis

INTRODUCTION

The vermiform morphology of the unicellular parasite *Trypanosoma brucei* that causes African trypanosomiasis in humans and nagana in cattle is defined by a subpellicular array of microtubules

(MTs) (Robinson *et al.*, 1995; Gull, 1999; Wheeler *et al.*, 2013). These MTs are cross-linked to each other and the plasma membrane via regularly spaced fibrils (Sherwin *et al.*, 1987). A high order is maintained within the corset with the MT plus ends converging at the parasite's posterior end and the minus ends located at the anterior of the cell (Robinson *et al.*, 1995).

The only place where the continuity of the *T. brucei* MT array is interrupted is at the flagellar pocket, the deep invagination where the flagellum exits the cell body and the only place where endo- and exocytoses occur (Field and Carrington, 2009). The opening of the flagellar pocket is encircled by a collar, which influences the overall shape of this cavity. Distal to the collar, the so-called hook complex covers the flagellum as it exits the flagellar pocket, with two lateral arms also flanking the flagellum attachment zone (FAZ) filament and the MT quartet (MtQ) inside the cell (Albisetti *et al.*, 2017). The FAZ filament and MtQ are among the interconnected fibres, filaments and junctional complexes of the multipartite FAZ (Lacomble *et al.*, 2009), which together form a lateral attachment for the flagellum as it follows a helical path along the cell body, connecting the flagellar skeleton to the cytoskeleton through both the flagellar and plasma membranes (Sunter and Gull, 2016). The MtQ originates close to the basal bodies, wraps itself around the flagellar pocket and interdigitates within the MT corset next to the FAZ filament. The orientation of MTs in the MtQ is antiparallel to the one found within the MT corset, thus their minus ends are proximal to the basal bodies (Robinson *et al.*, 1995).

The trypanosome MT corset is exceptionally stable and only reorganised during cell division and life cycle transitions (Sinclair and de Graffenried, 2019). Cytoskeletal structures (MtQ, MT corset, flagellum, basal bodies, which anchor the flagella within the cell, and FAZ) need to be duplicated and faithfully segregated during the cell division cycle, just like other single-copy organelles. In addition, this has to be coordinated with replication and division of the nucleus and the single mitochondrial DNA network termed the kinetoplast, which is located on the opposite side of the basal bodies relative to the flagellum (Robinson *et al.*, 1995; Wheeler *et al.*, 2019).

Basal body duplication and segregation are the first visible steps in the cell division cycle and essential for subsequent cytokinesis (Woodward and Gull, 1990). The new MtQ starts growing just prior to basal body maturation and once the new flagellum has grown enough to invade the flagellar pocket, morphogenetic changes result in two separate pockets enveloping both the new and old flagella (Lacomble *et al.*, 2010). Once the new flagellum has been nucleated and elongated, new MTs are integrated into the array between the old and new flagella, thereby increasing the overall width of the cell (Wheeler *et al.*, 2013).

With its antiparallel orientation, the MtQ together with the FAZ filament create an asymmetric seam within the MT corset, which works as a 'cellular ruler' and helps to determine the site of future furrow ingression during cytokinesis (Sunter and Gull, 2016). Any insults to the integrity of these structures result in cytokinesis defects and it is thus tempting to envision the MtQ as a potential specialised 'highway' in charge of transport and delivery of cargo to the site of important cytokinesis events. Furthermore, the endplasmic reticulum associates with parts of the MtQ, although the importance of this association remains mysterious. The first protein localized to this structure, TbSpef1, is found at the proximal end of the MtQ, which wraps around the flagellar pocket between basal bodies and the flagellar pocket collar (Gheiratmand *et al.*, 2013). Its depletion causes problems with the biogenesis of the MtQ and associated structures as well as motility defects. The minus end of the MtQ MTs is anchored to the basal bodies by a protein named TbSAF1, found in close proximity to TbSpef1 but localized between the pro and mature basal bodies (Dong *et al.*, 2020). TbSAF1 was found in a proximal proteomics screen of proteins adjoining to and/or directly interacting with TbSpef1, which found three additional proteins that localize to the MtQ between the basal body and

83 flagellar pocket collar (Dong *et al.*, 2020). However, no motor proteins that localise to the MtQ, and
84 which may potentially bring cargo to the cytokinesis site, have thus far been identified.

85 Kinesins are well-studied motor proteins that regulate MT dynamics, organize MT networks, and
86 transport cargo along MTs. Transporting kinesins can form homo- and heterodimers and consist of a
87 head region containing the kinesin motor domain, which is responsible for ATP hydrolysis and MT
88 binding, and a tail region important for dimerization with a kinesin/kinesin-like partner and cargo
89 binding (Hirokawa and Noda, 2008). In trypanosomatid genomes, kinesins and kinesin-like proteins
90 constitute one of the largest protein superfamilies (Berriman *et al.*, 2005; El-Sayed *et al.*, 2005; Ivens
91 *et al.*, 2005). To date, 47 genes encoding high-likelihood kinesins have been identified in the *T. brucei*
92 genome (Wickstead and Gull, 2006; Wickstead *et al.*, 2010b). Moreover, there is a similar number of
93 kinesin-related proteins, which did not make the threshold due to sequence variance (Berriman *et*
94 *al.*, 2005). Interestingly, numerous kinesins are members of two major clades named X-1 and X-2
95 that are restricted to the trypanosomatid lineage (Wickstead and Gull, 2006; Wickstead *et al.*,
96 2010b). Why the kinesin repertoire has expanded so prominently in trypanosomatids remains
97 mysterious.

98 Hitherto studied kinesins of *T. brucei* have been shown to be important for various processes
99 occurring in different cellular compartments. KinA and KinB are involved in cell cycle progression and
100 localise to the central spindle during mitosis (Li *et al.*, 2008) while TbKif13-1 localizes either to the
101 nucleus or the mitotic spindle, where it meditates chromosome segregation during mitosis
102 (Wickstead *et al.*, 2010a). KinC and KinD are distributed throughout the cytoskeleton, where they are
103 involved in subpellicular MT organization, basal body segregation and cytokinesis (Hu *et al.*, 2012;
104 Wei *et al.*, 2013).

105 Some kinesins are associated with the flagellum and adjacent FAZ. KIN2A and KIN2B are kinesins
106 involved in intraflagellar transport, a process that directly affects flagellar assembly and in turn
107 affects cell motility and cytokinesis (Aslett *et al.*, 2009; Bertiaux *et al.*, 2020). The orphan kinesin KIN-
108 E predominantly localises to the flagellar tip and is required for elongation of the new FAZ (An and Li,
109 2018). Another orphan kinesin named KLIF initially localises to the tip of the new, elongating FAZ and
110 associates with the old FAZ as the cytokinetic furrow ingresses towards the posterior end, thus
111 mediating the final stages of cytokinesis (Hilton *et al.*, 2018). Other kinesins localising to specific
112 cytoskeletal structures include FCP2/TbKinX1 and FCP4/TbKin15, which are found at the flagella
113 connector (FC), a trypanosome-specific structure that connects the outgrowing new flagellum to the
114 old one (Varga *et al.*, 2017). Interestingly, FCP2/TbKinX1 belongs to kinesin clade X1, one of the two
115 trypanosomatid-restricted kinesin families (Wickstead and Gull, 2006; Wickstead *et al.*, 2010b).

116 Here we present data on the localisation and function of two members of the kinesin superfamily,
117 TbKifX2A and TbPH1, with the former protein belonging to clade X2. Functional characterization and
118 the unique localization of these kinesins further expands our knowledge on how these diverse and
119 dexterous proteins affect the biology of these extremely diverse and successful parasites.

120

121 **RESULTS**

122 **TbPH1 is a kinesin-like protein that fractionates with the *T. brucei* cytoskeleton**

123 TbPH1 (Tb927.3.2490) is a 110 kDa protein named after a C-terminal pleckstrin homology (PH)
124 domain, which is followed by a proximate homeodomain-like (HDL) fold and preceded by a coiled
125 coil (CC) domain (Fig. 1A). The protein undergoes post-translational modifications, with

126 phosphorylation of a serine at the start of the HDL (Urbaniak *et al.*, 2012) and a methylarginine in
127 the middle of the primary structure (Lott *et al.*, 2013). While TbPH1 has an N-terminal kinesin motor
128 domain, two substitutions of highly conserved amino acids within the Walker A motif (G93P and
129 T/S95R) likely ablate the ATP hydrolase activity. Thus, TbPH1 is unlikely to be a *bona fide* kinesin
130 motor protein**.**

131 TbPH1 also belongs to the ~2000 proteins found in the granule-enriched fraction (containing cellular
132 aggregates, nuclei, kinetoplasts and flagella as well as associated cytoskeletal structures) obtained
133 by 'MT sieving', a method originally conceived to purify stress granules from *T. brucei* (Fritz *et al.*,
134 2015). In brief (see S1 Fig. for 'MT sieving' pipeline), cells are lysed by non-ionic detergent in low
135 ionic strength buffer, which maintains the cytoskeleton, including the MT corset that in turn cages
136 predominantly detergent insoluble cellular structures with at least one dimension >20-30 nm. The
137 MT corset is then disrupted by 300 mM NaCl to release these elements for subsequent analysis.

138 To verify TbPH1's apparent association with cytoskeletal fractions, we subjected a *T. brucei* cell line
139 in which the endogenous *TbPH1* open reading frame was appended with a C-terminal V5 tag (Dean
140 *et al.*, 2015) to cell fractionation by a procedure identical to 'MT sieving'. The cell equivalents of the
141 ensuing fractions were inspected for the presence of TbPH1-V5 and SCD6, a stress granule marker
142 that served as a control for this method (Fig. 2A). SCD6 was mostly found in the soluble fractions as
143 previously reported for unstressed *T. brucei* (Fritz *et al.*, 2015), with a distribution across the
144 analysed fractions very distinct from that of TbPH1-V5. TbPH1-V5 was well retained in all
145 cytoskeletal fractions P1 and P2, although a fraction was released in the SN1 with other soluble
146 cytosolic proteins upon initial lysis (Fig. 2A). Importantly, an aliquot of P2 fraction that was fixed on
147 microscopic slides for indirect immunofluorescence (IFA) using an anti-V5 antibody shows that
148 TbPH1-V5 is localized as a line extending from the DAPI-stained kinetoplast (Fig. 2B) that decreases
149 in signal intensity distally, suggestive of a cytoskeletal localization. This was confirmed by the
150 observation that the vast majority of TbPH1 was released into the soluble SN3 fraction after high salt
151 disintegration of the cytoskeleton. A small amount of TbPH1-V5 was still found in the final pellet P3,
152 which is consistent with its detection in the cohort of proteins retained by 'MT sieving' (Fritz *et al.*,
153 2015). Thus, a significant portion of the kinesin-like protein TbPH1 fractionates with the
154 trypanosomal cytoskeleton.

155 **TbPH1 strongly interacts with the trypanosomatid-restricted orphan kinesin TbKifX2A**

156 Because kinesins tend to form dimers (Marx *et al.*, 2009) and kinesin-like TbPH1 contains a CC
157 domain (Fig. 1A), which usually mediates protein-protein interactions (Burkhard *et al.*, 2001), we
158 proceeded to see if TbPH1-V5 has an interaction partner by immunoprecipitation (IP) via its C-
159 terminal epitope tag. To enrich for soluble TbPH1-V5 and augment IP stringency, we followed the
160 previously described fractionation technique and used fraction SN3 as the input (Fig. 3A). A mock IP
161 control using the parental cell line without an expressed V5 epitope was performed in parallel.

162 After confirming immunocapture of TbPH1-V5 in the first eluate (Fig. 3A), the IP eluate from this and
163 the mock control were resolved on a SDS PAGE gel. Sypro Ruby protein gel staining showed two
164 prominent bands of ~117 kDa (Fig. 3B, B1), the expected size for TbPH1-V5, and of ~80 kDa (Fig. 3B,
165 B2). Importantly, these bands were not observed in the mock control, indicating their presence is
166 not due to unspecific binding to the magnetic beads used to immobilize the anti-V5 antibody. Mass
167 spectrometry analysis of these two excised bands identified TbPH1 itself as expected and a
168 previously uncharacterised kinetoplastid-specific kinesin (Tb927.9.15470) (S1 Dataset), which we call
169 TbKifX2A based on a previously proposed kinesin nomenclature (Wickstead *et al.*, 2010b). In contrast
170 to TbPH1, TbKifX2A's kinesin motor domain contains a conventional Walker A motif (Fig. 1A). This

171 motor domain is located on the N-terminus, indicating that TbKifX2A actively moves toward the
172 plus-end of MTs (Hirokawa *et al.*, 2009). It also contains a CC domain and two serine
173 phosphorylation sites (Urbaniak *et al.*, 2012), similarly to TbPH1.

174 Interaction between these two proteins was further verified by tagging TbKifX2A with a C-terminal
175 HA tag in the TbPH1-V5 cell line. Indeed, TbKifX2A mirrored the fractionation pattern of TbPH1-V5
176 (Fig. 3C). As before, the SN3 fraction was used as an input for TbKifX2A-HA IP, which co-
177 immunoprecipitated TbPH1-V5. Thus, we verified that TbPH1 and TbKifX2A exhibit a strong
178 interaction that persists even in 300 mM NaCl.

179 Whole cells expressing TbPH1-V5 and TbKifX2A-HA were fixed and permeabilized prior to incubation
180 with antibodies recognizing either epitope-tag (Figs. 3D and E). We observed that both proteins
181 possess a considerable cell body signal that appears to be nucleus-excluded, with a prominent signal
182 along the proximal region of the flagellum. This pattern is similar to the TrypTag localization data,
183 which visualized mNeonGreen-tagged proteins in immobilized live cells (Dean *et al.*, 2017). The cell
184 body signal likely represents the cytosolic population of both proteins that was also observed in our
185 fractionation data (Figs. 2A and 3C). It should be also noted that TbPH1-V5 only also displays an
186 increased signal on the anterior tip of the cell body (Fig. 3D, asterisks). Co-localisation of TbPH1 and
187 TbKifX2A in whole cells showed these two proteins to mainly associate with each other along the
188 proximal region of the flagellum (Fig. 3F).

189 **TbPH1 and TbKifX2A localize to the microtubule quartet within the cytoskeleton**

190 We next decided to address whether TbPH1 and TbKifX2A localize to or near the FAZ, as suggested
191 by the most prominent signal obtained in whole cell IFAs. Cytoskeletons were detergent-extracted
192 from the TbPH1-V5 and TbKifX2A-HA expressing cells to visualize any potential localization to
193 discrete cytoskeletal structures. Indeed both proteins co-localized to a long structure running along
194 the long-axis of the cytoskeleton adjacent to the flagellum (Figs. 4A and S2A). Furthermore,
195 detergent extraction solubilized the cell body signal (Figs. 3D, E and F), confirming it represented the
196 cytosolic population of TbPH1 and TbKifX2A (Figs 2A and 3C). The specificity of the antibodies
197 recognizing V5 and HA on extracted cytoskeletons was verified by a lack of signal in the parental cell
198 line lacking either of these epitopes (Fig. S2B).

199 We proceeded to identify specifically which cytoskeletal element TbPH1 and TbKifX2A associate
200 with. We used antibody recognizing TbKifX2A-HA as a proxy for the TbKifX2A-TbPH1 complex
201 because of their demonstrated tight interaction (Fig 3), and their co-localization on detergent-
202 extracted cytoskeletons (Fig4A, S2A). We note that in contrast to the TbPH1 co-localization assay
203 depicted in Figs. 4A and S2A, we used rabbit antibody recognizing the HA tag to allow us to
204 counterstain with antibodies raised in mouse and rat.

205 We found that TbKifX2A-HA exhibited a strong signal further toward the proximal region of the
206 flagellum that tapered in signal intensity in a line juxtaposed with the FAZ filament (Figs. 4B and
207 S2D). This region of strong TbKifX2A-HA signal co-localized with the basal bodies (Figs. 4C and S2C).
208 This pattern led us to investigate whether the kinesin was bound to the MtQ, as it originates close to
209 the basal body and is considered a part of the FAZ (Lacomble *et al.*, 2009; Sunter and Gull, 2016). To
210 this end, we used the monoclonal antibody 1B41 recognizing the MtQ (Gallo *et al.*, 1988), a
211 somewhat contentious claim that is belied by its use as a MtQ marker in subsequent studies
212 (Rotureau *et al.*, 2011) (see Experimental Procedures for more details about the 1B41 batch used
213 here). Indeed, TbKifX2A-HA shows co-localization with 1B41 (Figs. 4D and S2E), suggesting that
214 TbKifX2A may associate with the MtQ.

215 To verify that TbKifX2A indeed binds the MtQ, we employed expansion microscopy (ExM), which
216 enlarges cells by embedding them within a swellable polyacrylamide matrix prior to immunolabelling
217 to allow examination of cellular structures in greater detail (Gambarotto *et al.*, 2019). ExM has
218 recently been implemented in *T. brucei* (Gorilak *et al.*, 2021; Amodeo *et al.*, 2021), and accentuates
219 the part of MtQ that wraps around the flagellar pocket upon immunolabeling with antibody
220 recognizing MT-incorporated, acetylated α-tubulin (Fig. 5A) (Gorilak *et al.*, 2021). Additionally, this
221 procedure allows the proximal MtQ to be distinguished from the nearby hook complex, which lacks
222 MTs (Esson *et al.*, 2012).

223 Performing ExM allowed us to localize TbPH1-V5 or TbKifX2A-HA to the part of the MtQ that spirals
224 around the flagellar pocket, as demonstrated by the co-localization of each epitope tag with
225 acetylated α-tubulin in both 3D reconstruction of expanded cells and individual focal planes (Figs.
226 5A-F). The associated V5 or HA signal was not discernible beyond the point of the MtQ joining the
227 corset MTs, where the signal of FAZ constituents, such as ClpGM6 (Hayes *et al.*, 2014), starts (Fig.
228 S3). The fact, that the signal of TbPH1-V5 or TbKifX2A-HA was apparent only in the part of the MtQ
229 around the flagellar pocket is consistent with this being the region of the highest concentration of
230 both proteins in the cell based on IFA (Figs. 3D-F), as well as with a lower sensitivity of ExM due to
231 dilution of epitopes stemming from specimen expansion. Taken altogether, ExM reveals that TbPH1
232 and TbKifX2A localize to the MtQ element of the *T. brucei* cytoskeleton. Additionally, we observed a
233 punctate signal of anti-V5 or anti-HA antibody in the expanded cell body (Figs. 5C-F), consistent with
234 the significant cytosolic fraction of both proteins (Figs. 2A, 3C-F).

235 **Proximity proteomics reveals the interaction network of TbPH1 and TbKifX2A**

236 Since conventional IP of TbPH1-V5 under high salt conditions identified only TbKifX2A as its major
237 interaction partner, we sought a different method to identify potential cargo and/or interactors of
238 this putative kinesin complex. To do this, we tagged TbPH1 with a C-terminal biotin ligase 'BioID2'
239 (Kim *et al.*, 2016), appended with an HA tag (Pyrih *et al.*, 2020), to facilitate proximity-dependent
240 biotin identification (BioID) of neighbouring proteins. First, we determined by IFA on permeabilized
241 whole cells using anti-HA antibody that TbPH1-BioID2-HA localizes adjacent to the kinetoplast, which
242 was also observed for TbPH1-V5 (*c.f.* Figs. 2B and 6A). TbPH1-BioID2-HA also exhibited biotinylation
243 activity, as visualized by streptavidin-conjugated to Alexa Fluor 488 (Fig. 6A), in contrast to the
244 parental cell line lacking BioID2 (Fig. 6B). Thus, we confirmed that the chimeric protein is properly
245 localized and appears to biotinylate TbPH1 itself or proximal proteins.

246 Purification of biotinylated proteins was performed as described elsewhere (Morriswood *et al.*,
247 2013) (S4 Fig.). Western blotting revealed that the vast majority of TbPH1-BioID2-HA was present in
248 the soluble S1 fraction (Fig. 6C), which was used for subsequent analysis. At first glance, this result
249 appears to disagree with previous findings from the 'MT sieving' fractionation, which employs
250 comparable amounts of non-ionic detergent and buffers of low ionic strength; however, we should
251 emphasise that 'MT sieving' fractionation uses a different detergent for a shorter incubation time
252 and at a lower temperature in comparison to the BioID purification (see Methods), which likely
253 explains this difference.

254 Next, the S1 fraction was incubated with streptavidin-coated magnetic beads to capture biotinylated
255 proteins, which were subsequently trypsinized on beads prior to liquid chromatography-tandem
256 mass spectroscopy (LC-MS/MS). A mock control using the parental cell line lacking BioID2 expression
257 was processed in parallel. A total of 1,131 proteins were detected with high confidence in at least
258 one of three biological replicates (Andromeda Protein Score ≥20; >1 unique peptide per protein) (S2
259 dataset). Following imputation of missing values, seven proteins were shown to be preferentially

260 biotinylated by TbPH1-BioID2-HA, as visualised by plotting the -10 log t-test p value versus the t test
261 difference in a volcano plot (Fig. 6D). Statistically significant hits are found above the cut-off curve in
262 this plot.

263 TbKifX2A was the most enriched protein based on both parameters, consistent with its strong
264 interaction with TbPH1. As expected, TbPH1 is also among the enriched proteins, indicating that
265 TbPH1-BioID2-HA biotinylated itself and/or a nearby untagged, endogenous form. The sub-cellular
266 location of the five novel proteins was determined using the TrypTag protein localization resource
267 (Dean *et al.*, 2017). This allowed us to already exclude one of them (Tb927.10.12110) as a
268 contaminant, given its nuclear localization. After TbKifX2A, a flagellar pocket protein named FP45
269 (Tb927.9.9730) was the next most enriched proximal protein. Interestingly, FP45 is a soluble protein
270 that has been shown to associate with the membrane surrounding the flagellar pocket by
271 immunogold labelling in an independent study (Gheiratmand *et al.*, 2013). A putative flavin-
272 trafficking protein (Tb927.8.1950) was the next most abundant protein, but does not have a TrypTag
273 localization entry at this time. However, like TbPH1 and TbKifX2A, this protein was found among
274 those that come into proximity with TOEFAZ1 (alias CIF1, (Zhou *et al.*, 2018)), a protein that
275 associates with the tip of the extending FAZ (Fig. 6E) (Hilton *et al.*, 2018). Furthermore, IFA has
276 shown that that N-terminally tagged Tb927.8.1950 exhibited a strong signal in the vicinity of the
277 kinetoplast (Hilton *et al.*, 2018). The next most enriched protein was a putative kinesin with a C-
278 terminal PH domain (Tb927.6.2880), which is concentrated around the basal body according to
279 TrypTag. Based on phylogenetic analysis described in the next section, we dub this kinesin TbKifX2C.
280 Finally, two dynamin-like proteins named DLP1 (Tb927.3.4720) and DLP2 (Tb927.3.4760) were
281 moderately enriched. DLP1/2 are localized to the flagellar pocket, which is consistent with their
282 involvement in clathrin-mediated endocytosis (Morgan *et al.*, 2004; Benz *et al.*, 2017). DLP1/2 were
283 also identified among TOEFAZ1-associated proteins, albeit with lower confidence (Fig. 6E) (Hilton *et*
284 *al.*, 2018).

285 We chose the three most enriched proteins identified by TbPH1 proximity labelling (FP45, TbKifX2C
286 and Tb927. 8.1950) for IP experiments to verify if they represent true interactors. Cells were lysed in
287 the same buffer as for the BioID procedure to maintain consistent conditions, except for
288 Tb927.8.1950. Because this protein appeared to be cleaved in the BioID buffer, a different buffer
289 that maintained the full-length protein was used for pull-down of this protein (Fig. S5). IP of the
290 three V5 baits was successful, but TbPH1-BioID2-HA co-IP was detected only in the FP45 or TbKifX2C
291 IPs (Fig. 6F, S5). FP45 exhibits a robust interaction with TbPH1-BioID2-HA, as the latter is noticeably
292 depleted from the flow through fraction, which contains unbound proteins. In contrast, it appears
293 that a fraction of TbKifX2C interacts with TbPH1, as there is a substantial amount of unbound TbPH1-
294 BioID2-HA in the flow through. TbPH1-BioID2-HA was not detected in any of the mock IPs or the
295 Tb927. 8.1950 IP. Thus, we conclude that FP45 and kinesin TbKifX2C are genuine TbPH1 interactors.

296 We also compared the TbPH1 proximity proteome to those of TbMORN1, a protein that is part of the
297 hook complex (Morriswood *et al.*, 2013), and TbSpef1, a protein localized to the MtQ (Dong *et al.*,
298 2020) (Fig. 6G). Tellingly, there was no overlap among any of these proteomes, suggesting that
299 TbPH1 is not in close proximity to TbMORN1 or TbSpef1 since the biotinylation radius of the BioID
300 biotin ligase is approximately 10 nm (Kim *et al.*, 2014).

301 **TbPH1 interacts with another X2 family kinesin in addition to TbKifX2A**

302 Because we demonstrated that TbPH1 interacts with a kinesin other than TbKifX2A, we decided to
303 further classify this protein, an effort that eventually led us to name it TbKifX2C. In the
304 comprehensive survey of kinesins (Wickstead *et al.*, 2010b), TbKifX2C was deemed too divergent to

305 group into any kinesin family. Nevertheless, it does bear a canonical N-terminal, kinesin motor
306 domain and a PH domain on its C-terminus (Fig. 1B). Furthermore, there is evidence that TbKifX2C is
307 phosphorylated, like TbPH1 and TbKifX2A (Fig. 1A) (Urbaniak *et al.*, 2012).

308 We noticed that the gene encoding TbKifX2C was syntenic to a *Leishmania major* gene encoding a
309 kinesin placed in the X2 clade (Wickstead and Gull, 2006; Wickstead *et al.*, 2010b). To get initial
310 support that TbKifX2C is part of the X2 family, we performed a BLASTP search of 12 predicted
311 proteomes covering trypanosomatid diversity (Lukeš *et al.*, 2018) (Table S1A) using TbKifX2A as a
312 query. A total of 47 protein entries were retrieved below the E-value threshold of 1e-20 (Table S1B).
313 TbKifX2C was in this dataset along with expected hits (*e.g.* orthologs of TbKifX2A).

314 Encouraged by this result, we next proceeded with an unbiased molecular phylogenetic approach to
315 test TbKifX2C's placement within the X2 family. We retrieved from the 12 predicted proteomes 549
316 sequences matching the Pfam 'kinesin motor domain' model in a hidden Markov Model search
317 (Table S1C, Supplemental data 1). These sequences were used to produce a trimmed alignment in
318 which extensive gaps were removed. This alignment was then used to construct the phylogenetic
319 tree depicted in Fig. 7A.

320 The majority of X2 family kinesins as defined by Wickstead and colleagues (Wickstead and Gull,
321 2006; Wickstead *et al.*, 2010b) were grouped into a well-supported clade that was comprised of
322 three distinct and well-supported sub-clades. Each sub-clade contained at least one annotated X2
323 family kinesin, such as TbKifX2A. Importantly, TbKifX2C was placed into the X2 clade as well,
324 clustering with the product of the syntenic *L. major* gene. It should be noted that sequences from
325 the basal trypanosomatid *Paratrypanosoma confusum* (Skalický *et al.*, 2017) represented early
326 diverging outgroups in all of the subclades except X2C, which contains the apparently divergent
327 sequences from *Trypanosoma* species. As a testament to this, the *Trypansoma congolense* member
328 of the X2C clade (TcIL3000_6_2380), which clusters with the divergent TbKifX2C, was the only X2
329 family sequence not retrieved in the initial BLASTP search (Table S1B). Thus, we conclude from these
330 unbiased *in silico* approaches that like TbKifX2A, TbKifX2C is a member of the X2 family.

331 To see if TbKifX2C co-localizes with TbPH1, we performed IFA on fixed whole cells and extracted
332 cytoskeletons (Fig. 7B-C). The signals from both TbKifX2C-V5 and TbPH1-BioID2-HA were enriched in
333 the vicinity of the kinetoplast in whole cells, where they clearly overlaid (Fig. 7B). TbKifX2C IFA signal
334 partially overlaps with TbPH1 at the part of extracted cytoskeletons near the retained kinetoplast
335 (Fig. 7C), which is consistent with a portion of TbPH1 interacting with TbKifX2C (Fig. 6F). This partial
336 co-localization is in contrast with the almost complete overlap of TbPH1 with TbKifX2A, which
337 indicates that TbKifX2A is the main partner of TbPH1, perhaps explaining why TbKifX2C was not
338 detected in the initial TbPH1 co-IP under the high salt conditions of 'MT sieving'.

339 To further explain why TbKifX2C was not observed in our initial IPs identifying the TbPH1-TbKifX2A
340 complex, we decided to look at expression of the *T. brucei* X2 family kinesins in long slender
341 bloodstream and procyclic stages (Tinti *et al.*, 2022). While TbPH1 is minimally regulated between
342 the two life cycle stages, TbKifX2A is considerably upregulated in the procyclic stage whereas
343 TbKifX2C is expressed at roughly a third of the levels as it is in the long slender stage (Fig. 7D).
344 Interestingly, the *T. brucei* kinesin belonging to the X2B sub-clade (Tb927.8.4840) exhibits more
345 regulated expression in the long slender stage, with only 1 peptide detected in the procyclic stage.
346 Thus, it appears that TbKifX2A is the predominant X2 kinesin in the procyclic stage, which was the
347 experimental model used in this study, which may also explain why this was the only kinesin to be
348 bound to TbPH1 during 'MT sieving'.

349 **Depletion of TbPH1 and TbKifX2A causes prominent morphological defects**

350 To assay the function of the novel kinesin TbKifX2A and its associated kinesin-like protein TbPH1, we
351 depleted their expression by doxycycline-induced RNAi in the cell line expressing TbPH1-V5 and
352 TbKifX2A-HA. The downregulation of either protein alone only marginally affected the growth of *T.*
353 *brucei* in comparison to the non-induced cells, despite efficient depletion of each of the respective
354 tagged proteins (Fig. 8A, Fig. S6A). Interestingly, TbPH1 levels were also depleted in the TbKifX2A
355 RNAi cell line (Fig. 8A, inset), suggesting that the protein might depend on its partner for stability.

356 To get a more robust RNAi phenotype for phenotypic analysis, we generated a cell line in which both
357 proteins were downregulated, which showed more pronounced growth inhibition than the single
358 knock-downs (Fig. 8B, Fig. S6A). Growth slowed after 3 days of RNAi induction and did not reach
359 levels of the uninduced counterparts at any point during the 7 day time course (Fig. 8B). Depletion of
360 both proteins was confirmed by western blotting (Fig. 8B, inset), although neither protein was
361 decreased below the detection limits of this assay, perhaps explaining the lack of a more severe
362 growth phenotype.

363 Because both TbPH1 and TbKifX2A are modified in a way suggestive of post-translational regulation
364 (Fig. 1A), we wondered whether the growth inhibition of the double RNAi knockdown is due to a cell
365 cycle defect. Thus, we assayed the proportion of cell cycle stages present over a course of 7 days of
366 TbPH1/TbKifX2A depletion, sorting individual DAPI-stained cells into different cell cycle stages by
367 scoring their number of nuclei (N) and kinetoplasts (K) (Robinson *et al.*, 1995). While we observed a
368 moderate decrease in 1N1K cells and increase in 2N2K cells (Fig. 8C), these were not to the extent
369 that would correspond to an unequivocal cell cycle defect. The number of zoids (cells with 1
370 kinetoplast and lacking a nucleus) reached a peak at day 5, making up about 7% of the population,
371 which may suggest a cytokinesis defect. However, a conclusive cytokinesis defect phenotype should
372 also include a concurrent emergence of 2N1K or multinucleated cells, which was not observed here
373 (Robinson *et al.*, 1995).

374 The cell cycle was also assayed by flow cytometry on propidium iodide-stained cells, which quantifies
375 the portion of cells in the G1, S and G2/M phases, as well as cells with aberrant DNA content
376 (Darzynkiewicz *et al.*, 1999). While the aforementioned cell cycles phases were not markedly
377 affected upon TbPH1/TbKifX2A depletion, this assay also revealed the statistically significant
378 emergence of zoids from three days post-induction (Fig 8D, Fig. S6C). Thus, while we cannot
379 conclude that TbKifX2A and TbPH1 play a direct role in cell cycle progression or cytokinesis, the two
380 assays we employed here indicate that their depletion leads to a slight accumulation of anucleate
381 zoids.

382 To gain unbiased insight into potential effects of simultaneous depletion of TbPH1 and TbKifX2A, we
383 prepared whole cell lysates after three and five days of induction and compared them to their
384 uninduced counterparts by LC-MS/MS. A total of 2,624 high-confidence proteins (using similar
385 criteria as for BioID LC-MS/MS, namely an Andromeda Protein Score ≥10 and >1 unique peptide per
386 protein) were detected for the three and five day time points, respectively. Reassuringly, TbPH1 and
387 TbKifX2A were the most downregulated proteins at both time points as targets of RNAi-depletion
388 (Fig. 9A). Furthermore, only two other proteins were consistently depleted at the two time points:
389 FP45 and TbKifX2C, the two direct interactors of TbPH1. The dependence of FP45 and TbKifX2C's
390 stability on the presence of TbPH1 and/or TbKifX2C underscores the interaction among these
391 proteins. Interestingly, a histidine phosphatase family protein (Tb927.11.11750) is the only
392 significantly upregulated protein at both time points.

393 We next addressed whether simultaneous downregulation of TbPH1 and TbKifX2A affects
394 cytoskeletal elements and the gross morphology of the cells. We assayed the MtQ and FAZ by IFA
395 after five days of RNAi depletion and observed no defects in either of these structures, indicating
396 that TbPH1 and TbKifX2A do not play a role in their biogenesis (Fig. S6B). However, by phase contrast
397 microscopy we noticed the expansion of the flagellar pocket (Fig 9B). In contrast to the mean
398 472±192 nm diameter observed in 120 uninduced control cells, the flagellar pocket diameters
399 expanded to 655±225 nm and 932±516 nm after three and five days of RNAi-induction, respectively,
400 indicating that the severity of this phenotype increases during the RNAi-time course. In conclusion,
401 simultaneous depletion of TbPH1 and TbKifX2A results in the expansion of the flagellar pocket, a
402 morphological phenotype that is congruent with TbPH1 and TbKifX2A's proximal MtQ localization.

403 We also noticed that at five days of RNAi-inductions, some cells exhibited protrusions extending
404 from the posterior end. To better visualize these phenotypes, we observed these cells by scanning
405 electron microscopy (Fig. 9C). While control cells showed normal trypomastigote morphology (Fig.
406 9C), we regularly observed cells with multiple protrusions (arrows) originating from the posterior
407 end in the induced population (Fig. 9C). The emergence of this phenotype was quantified from >380
408 cells in SEM pictures for both induced and uninduced populations of cells. While this phenotype only
409 occurred in about 5.4% of cells, this still represents a 10-fold increase versus non-induced cells (Fig.
410 9C). The occurrence of these cell types was also corroboratively found in transmission electron
411 microscopy, which in addition provided evidence that these protrusions appear to contain normal
412 cellular contents and were surrounded by subpellicular MTs (Fig. S7A).

413 This effect of TbPH1/TbKifX2A-depletion resembled the RNAi-phenotype of two tubulin-tyrosine-
414 ligase-like (TTLL) proteins, which post-translationally modify the C-terminal tails of α- and β-tubulin
415 by addition of polyglutamate side chains (Jentzsch *et al.*, 2020). Upon depletion of either TTLL,
416 protrusions were observed emanating from the posterior end, which prompted the authors to name
417 this morphological change the 'glove' phenotype. To investigate whether TbPH1/TbKifX2A
418 downregulation truly phenocopies that of each TTLL, we immunolabelled cells five days post RNAi-
419 induction with antibodies recognizing glutamyl side chains (GT335 antibody). Upon depletion of
420 either TTLL, polyglutamylation was decreased and α-tubulin tyrosination increased in the posterior
421 end, from which the protrusions emerged (Jentzsch *et al.*, 2020). We did not observe any changes in
422 polyglutamylation upon TbPH1/TbKifX2A silencing by imaging individual cells by IFA or on the
423 population level by western blot analysis (Fig. S7B), suggesting the mechanism underlying the
424 emergence of posterior-end protrusions differs from that of the TTLLs.

425

426 **DISCUSSION**

427 Kinesins and related kinesin-like proteins constitute one of the largest protein families encoded by
428 the *T. brucei* genome (Berriman *et al.*, 2005) and are represented by diverse gene repertoires in
429 other trypanosomatids as well (El-Sayed *et al.*, 2005; Ivens *et al.*, 2005; Wickstead and Gull, 2006;
430 Wickstead *et al.*, 2010b). Among the eukaryotes, trypanosomatids have experienced one of the
431 largest expansions of the kinesin motor superfamily, suggesting these proteins endow trypanosomes
432 with unique biological properties, many of which still await elucidation (Berriman *et al.*, 2005;
433 Wickstead and Gull, 2006; Wickstead *et al.*, 2010b). Indeed, this expansion has resulted in the
434 emergence of two trypanosomatid-specific kinesin families named X1 and X2. A kinesin belonging to
435 the former, named FCP2/TbKinX1, has been shown to maintain a connection of a new flagellum's
436 distal tip along the side of the old flagellum, thus facilitating the unique mechanism of templated
437 flagellar replication in *T. brucei* (Varga *et al.*, 2017).

438 In this work, we have shed light on the thus far neglected X2 family of kinesins. First, by a widescale
439 phylogenetic analysis using kinesin sequences from 12 trypanosomatid species, we have shown that
440 the X2 family is comprised of 3 sub-clades. Sub-clades X2A and X2B contain kinesins from 11 of the
441 12 searched predicted proteomes, whereas X2C has representative from all 12. Thus, it appears that
442 the 3 sub-clades are well-conserved in trypanosomatids, with gene losses being the exception,
443 suggesting that this X2 kinesin repertoire is fundamental for these flagellates. Indeed, the model
444 used in this study, *T. brucei*, possesses kinesins from all three sub-clades.

445 The well-supported X2 clade of our study essentially agrees with the composition of the X2 clade
446 that was initially revealed in a phylogenetic tree of kinesins throughout eukaryotes, with one notable
447 exception (Wickstead and Gull, 2006; Wickstead *et al.*, 2010b). Two *L. major* and *T. brucei* kinesins
448 that were originally annotated as X2 family kinesins were placed outside of the X2 clade in our
449 analysis (marked 'X2?' in Fig 7A). This can be explained by the fundamental different datasets and
450 goals of the two studies. Wickstead and colleagues aimed to understand general kinesin evolution,
451 and thus sampled a wider range of eukaryotes, necessitating the inclusion of only two
452 trypanosomatid species. Our study aimed to address whether a divergent kinesin should be included
453 in the kinetoplastid-specific X2 family, and thus we restricted our dataset to a wider range of 12
454 trypanosomatid species. In the end, the trees are not as contradictory as they ostensibly seem at
455 first. The outlying kinesins in our 'X2?' clade were placed sister to the otherwise well-supported X2
456 clade with less than 50% support in Wickstead's tree (Wickstead and Gull, 2006), which is consistent
457 with the placement of these sequences in relation to the X2 clade in our study. Thus, we propose
458 that our tree reveals the structure of the X2 family *sensu stricto* (*s.s.*), given the level of support of
459 this clade and contained sub-clades, implying the stability of its internal branching. The evolution of
460 the kinesin superfamily in kinetoplastids is out of the scope of this study, but we hope this result
461 provides impetus for future investigation of this topic.

462 Another property of X2 *s.s.* kinesins we have serendipitously discovered in this study is that they
463 directly interact with TbPH1, a likely catalytically-dead, kinesin-like protein with a C-terminal PH
464 domain that localizes to the MtQ. While we do not address here whether TbPH1 has truly lost ATP
465 hydrolase activity, it contains two point mutations to conserved residues of the Walker A motif that
466 are likely to ablate this activity. A glycine to proline mutation exchanges the amino acid that confers
467 the most flexibility to the peptide backbone for one that rigidifies it. The polar threonine/serine
468 amino acid responsible for the requisite coordination of Mg^{2+} (Deltoro *et al.*, 2016) is replaced with a
469 positively charged arginine, which would repel this cation. Divergent Walker A motifs that still retain
470 ATP hydrolase activity do not have two such mutations at once (Hu *et al.*, 2012; Deltoro *et al.*, 2016).
471 Thus, the notion that TbPH1 has an inactive kinesin motor domain is likely but empirically unproven.

472 We show that TbPH1 very tightly interacts with TbKifX2A in a manner persisting even at high ionic
473 strength. This interaction most likely occurs at the part of the MtQ wrapped around the flagellar
474 pocket, where both proteins are considerably enriched. TbPH1 and TbKifX2A exhibit a cytosolic pool
475 as well, but it remains unknown to what extent if at all they interact away from the MtQ. Proximity
476 labelling revealed two more direct interactors of TbPH1: FP45, a protein that localizes to the flagellar
477 pocket (Gheiratmand *et al.*, 2013) and surprisingly another X2 family *s.s.* member, TbKifX2C.
478 Furthermore, the stability of both proteins is dependent on the presence of TbPH1 and/or TbKifX2A,
479 indicating the interdependence of these proteins that are all enriched in the vicinity of the flagellar
480 pocket associated MtQ.

481 TbPH1's interaction with FP45 may explain the primary phenotype we have observed upon
482 simultaneous downregulation of TbKifX2A and TbPH1: the expansion of the flagellar pocket. This
483 phenotype is congruous with the localization of TbPH1 interactors and may be a consequence of the

484 subsequent depletion of FP45. Unfortunately, we are not able to corroborate this result as
485 regulatable RNAi-cell lines targeting FP45 were reported to be unstable, precluding functional
486 analysis (Gheiratmand *et al.*, 2013). Indeed, we have also encountered problems in obtaining robust
487 phenotypes downregulating TbPH1 and TbKifX2A individually or simultaneously upon extended
488 growth and/or cryopreservation. Thus, from our and other's experience, complete ablation of this
489 cohort of MtQ-associated proteins is difficult, which complicates their functional analysis.

490 We have also observed some morphological defects affecting a minor proportion of cells upon
491 TbPH1/TbKifX2A downregulation that are at this time difficult to explain. One is the emergence of
492 anucleate zoids, intensifying at the same RNAi time point when we observe the flagellar pocket
493 expansion. At this time, we rule out that this is due to cytokinesis defects, as this would also give rise
494 to a more conspicuous enrichment of 2N1K or multinucleate cells, which we did not observe. In the
495 final RNAi time point examined here, we also observed cells exhibiting posterior-end protrusions,
496 resembling the 'glove phenotype' observed upon depletion of two TTLL enzymes, which are
497 responsible for post-translational modifications appending the C-terminal tails of α- and β-tubulin
498 (Jentzsch *et al.*, 2020). As neither TTLL12A (TTLL6A was not among the detected proteins, Dataset
499 S3) nor the modifications both enzymes catalyse are affected by TbPH1/TbKifX2A-silencing, we
500 conclude that these protrusions arise from a different mechanism.

501 Altogether, we conclude that TbPH1 and TbKifX2A play a still undefined role in maintaining compact
502 flagellar pocket morphology. Whether one or both spuriously occurring defects are a direct
503 consequence of the primary flagellar pocket expansion phenotype or due to incomplete ablation of
504 TbPH1 and TbKifX2A remains unknown. Another possibility is that the cytosolic pool of TbPH1
505 and/or TbKifX2A may play a role in posterior end morphogenesis. What we can say is that it is
506 unlikely that they are arising from secondary depletion of proteins other than the targeted ones or
507 the downregulated TbKifX2C and FP45, as none of the other proteins detected in our LC-MS/MS
508 analyses are affected throughout the examined RNAi time course.

509 TbKifX2A is the first motor protein that has been demonstrated to localize to the MtQ. This and our
510 finding that TbKifX2C partially interacts with the MtQ-binding TbPH1 suggests the exciting possibility
511 that the X2 family *s.s.* kinesins co-evolved with the MtQ, a cytoskeletal component that is considered
512 to be part of the FAZ and restricted to trypanosomatids (Sunter and Gull, 2016). It has been
513 suggested that the MtQ contains β-tubulin with a unique but still unknown modification that is
514 recognized by the 1B41 monoclonal antibody (Gallo *et al.*, 1988; Gallo and Precigout, 1988), which
515 may at least partially explain why these kinesins and TbPH1 perferentially bind to the MtQ over the
516 corset MTs. This specificity may be mediated by interaction with TbPH1, perhaps explaining this
517 instance of a kinesin interacting with a catalytically-inactive kinesin-like protein. An example of this
518 phenomenon is the budding yeast Kar3 kinesin interacting with kinesin-like Vik1, which confers to
519 the Kar3/Vik1 complex a strong interaction with a microtubule (Allingham *et al.*, 2007).

520 Another striking feature of the three X2 family *s.s.* kinesin paralogs in *T. brucei* is their apparent
521 regulation in the long slender bloodstream and procyclic stages, with TbKifX2A being solely
522 upregulated in the latter. In contrast, TbPH1 exhibits more consistent expression levels between
523 these two stages. This suggests that the X2 *s.s.* kinesin repertoire is remodelled to adapt each stage
524 to their specific milieus. Perhaps this regulation is due to the higher endocytic flux in long slender
525 bloodstream forms in comparison to the procyclic forms, a process that occurs via the flagellar
526 pocket (Field *et al.*, 2009). This is certainly a worthy line of future investigation. Given that the X2
527 family *s.s.* kinesin may have co-evolved with the MtQ, it will be also interesting to see how the X2
528 kinesins have adapted to the presence of the cytostome-cytopharynx complex, an organelle that is
529 closely associated with the MtQ in *Trypansoma cruzi* (Alcantara *et al.*, 2017) and the basal

530 trypanosomatid *P. confusum* (Skalický *et al.*, 2017). Thus, our study represents a starting point for
531 investigation of this kinetoplastid-specific family of kinesins.

532

533 **EXPERIMENTAL PROCEDURES**

534 **Cells**

535 Procyclic SmOxP9 cells (Poon *et al.*, 2012) were grown in SDM79 with 1 µg/ml of puromycin. Cell
536 lines bearing epitope tags were grown with 50 µg /ml hygromycin (TbPH1-V5, FP45-V5, TbKifX2C-V5,
537 Tb927.8.1950-V5), 15 µg /ml G418 (TbKifX2A-HA) and 10 µg /ml blasticidin (TbPH1-BioID2-HA).
538 Selection for the RNAi constructs was with 2.5 µg /ml phleomycin (TbKifX2A RNAi, TbPH1 RNAi and
539 TbKifX2A+TbPH1 RNAi).

540 **Plasmids and generation of cell lines**

541 For epitope tagging at the endogenous locus with HA and V5, long PCR products were generated
542 with primers detailed in Table 1 using pPOT-V5-HygR and pPOT-HA-NeoR vectors as templates
543 (based on (Kaurov *et al.*, 2018) and modified from pPOTv4 (Dean *et al.*, 2015)). For tagging with the
544 BioID2 ligase (Kim *et al.*, 2016), a modified version of pPOTv7-Blast-mNG (Pyrih *et al.*, 2020) was
545 used as a template for TbPH1 endogenous locus tagging. 50 µl PCR reactions were directly
546 transfected into procyclic SmOxP9 cells using the Amaxa Nucleofactor electroporator and selection
547 occurred approximately 16 hours after electroporation.

548 Table 1

TbPH1V5_Fw	5'TTTCTTCCGGTCTTGACTTATTCCGCTCAGGGAAGCTTTATGATTTCTTATGCGAAAAGAGAGTCATACCGCTCCCGTACggttctggtagtggttcc-3'
TbPH1V5_Rv	5'ATAATAAAGAGGAAGGGAAGGTAAAGTTCAGAAACAAATTCTGTTGGCTCCTGATAACACTCTCATATTTCCTTCACCGCccaatttgagagacctgtg-3'
TbKifx2AHA_Fw	5'AACTACAGTTGCAAATGTGCATGATAGGAAGAAGTTGCCTCACGATGGAGCGTTGGAAAGCGGAACATGTCGGAACCGCAggttctggtagtggttcc-3'
TbKifX2AHA_Rv	5'CATTTTAAACAATTTCTCCTTCCCTCTTTTTTCACTCATTCATTCATTCATTCATTCACCACCTTCTTTTTTTTTTGCCTccaatttgagagacctgtg-3'
FP45_Fw	5'-TTCCACCGTATGGACCGTACGCTCCTTCAGCAAAGCTCATGGAGACGCTTGAGAAA AAATACAAGAAGCGTGCAGCGGCTggttctggtagtggttcc-3'
FP45_Rv	5'CTGTCCTACCTCGCCTCATCTTGGTAATGACGAAAAGCGAGACACCAACTGAAGATGACACCAAATGAGACAACGTGTGCccaatttgagagacctgtgc-3'
KifX2C_Fw	5'GGATGTTGTTTCAACAAATGAATCTTGTGTACGATGACAACTTCGTGCCGGCGACGACATTCGGTATCACTCGGCGGAGTggttctggtagtggttcc-3'
KifX2C_Rv	5'GATAATATAAGTTTGTCAAAGACACAAAACAGCAACGAAGTGTAAGGTGAAGACATAAATGATGGAGAAAAAAGAGAATAccaatttgagagacctgtgc-3'
Tb927.8.1950_Fw	5'CTGCTAACGAGTGCAGGTTTAATCAGACCGATCCTTGTAAGCTGCTTGTGCGCCCGGATGATGAGCGCCTCATCCCAGCTggttctggtagtggttcc-3'
Tb927.8.1950_Rv	5'TTAACCGCAAAAGGCATTACCTCCCCGTTATTCTCTCACACCTTACCCCAGGGCAACGCCCTCCTAAGTTGCAATATATAccaatttgagagacctgtgc-3'

549 To create a vector to simultaneously downregulate both TbPH1 and TbKifX2A, a fragment of each (as
550 suggested by RNAit2 software (https://dag.compbio.dundee.ac.uk/RNAit/) (Redmond *et al.*, 2003))
551 was PCR amplified using primers TbPH1-RNAi-Fw (TAATtctagaGTTGCGTGATGAGCTTCAAA), TbPH1-
552 RNAi-Rv (TATAaagcttCTCCTCTAGCACCGTTTTGC), TbKifX2A-RNAi-Fw (TAATggatccCACCGCCATTCTGCA
553 AACAA) and TbKifX2A-RNAi-Rv (TATAtctagaGTCATTTGCGTGGGCGATAC) and cloned into BamHI-
554 HindIII sites of p2T7-177 (Wickstead *et al.*, 2002) in a three way ligation using XbaI as the restriction
555 site in between the two RNAi fragments. The plasmid was linearized with NotI before
556 electroporation.

557 **RNAi and growth curves**

558 Procyclic form cell lines for depletion of either TbPH1 or TbKifX2A were induced at a density of $2x10^6$
559 cells/ml with 1 µg/ml doxycycline and growth monitored daily with a Z2 Coulter Counter Analyzer
560 (Beckman Coulter). Cells were diluted back to the initial cell density every day. Cell lines carrying the
561 vector for simultaneous depletion of TbPH1 and TbKifX2A were induced at a density of $5x10^5$
562 cells/ml with 1 µg/ml doxycycline and growth monitored daily with a Neubauer counting chamber.
563 Cells were diluted back to the initial cell density every two days.

564 **DAPI counts**

565 For cell cycle analysis, cells either induced or not for depletion of TbKifX2A and TbPH1 were spread
566 on glass slides, the cell suspension allowed to air-dry and the slides then fixed in methanol at -20 °C.
567 Slides were rehydrated for 5 minutes in PBS before a drop of ProLong™ Gold antifade reagent with
568 DAPI (ThermoScientific) was added, a coverslip applied and the slide sealed. At least 200 cells were
569 scored according to the number of nuclei and kinetoplasts per slide.

570 **Flow cytometry**

571 For flow cytometry, $1\text{-}2x10^6$ cells were fixed in 30% methanol-PBS at least overnight and up to seven
572 days at 4 °C. Samples were washed once in PBS-T (0.5% Triton) and subsequently incubated at 37 °C
573 for 1 hour in propidium iodide staining solution (10 µg/ml propidium iodide and 9.6 µg/ml RNaseA in
574 PBS-T, both from Sigma). Samples were analysed on a FACS Canto II (BD) collecting 50,000 events,
575 and data processed in FCSalyzer (https://sourceforge.net/projects/fcsalyzer/).

576 **Cell fractionation via 'microtubule sieving'**

577 To entrap non-soluble and cytoskeletal proteins within the MT corset, a MT sieving technique as
578 described in (Fritz *et al.*, 2015) was employed. The experiment was conducted exactly as described
579 before in (Fritz *et al.*, 2015) (see also Fig. S1).

580 **Immunoprecipitation**

581 For immunoprecipitation (IP) of TbPH1-V5 from procyclic trypanosome lysates, the V5 antibody
582 (Thermo Fisher) was coupled and cross-linked to protein G coated dynabeads (Thermo Scientific)
583 using 6 mg/ml dimethyl pimelidate dihydrochloride in 0.2M triethanolamine. Beads were then
584 washed in IP wash buffer (20 mM Tris-HCl, pH 7.7, 100 mM KCl, 3 mM $MgCl_2$, 0.5% TritonX-100,
585 cOmplete™ EDTA-free protease inhibitor (Roche)) and stored at 4 °C before further usage. For
586 proteomic analysis of TbPH1 interactions, $1x10^9$ PCF cells were pre-fractionated using the MT sieving
587 technique described above. The SN3 lysate was incubated with V5-coupled dynabeads for 24 hours
588 at 4 °C. Following several washes in IP wash buffer, proteins were eluted using low pH glycine buffer.
589 Aliquots were taken of the different steps for western blot analysis. For IP of TbKifX2A-HA the same

590 protocol was followed except that the antibody used was anti-HA (ThermoScientific) instead of anti-
591 V5.

592 For IP of potential TbPH1 interactors, $2x10^8$ cells expressing FP45-V5 and TbKifX2C-V5 in addition to
593 TbPH1-BioID2-HA were lysed and processed exactly as described in the BioID section below except
594 that the beads used were paramagnetic V5-Trap® beads (Chromotek). Samples corresponding to 2%
595 of the total (start and flow through fractions) and 20% of the total (beads fraction) were loaded on
596 SDS PAGE gels, blotted onto PVDF membranes and probed with anti-HA and anti-V5 antibodies as
597 described below.

598 Since full length Tb927.8.1950-V5 could not be recovered in the BioID lysis buffer, optimal lysis
599 conditions were determined by testing different buffers (B1: 10 mM Tris-Cl, pH7.8, 150 mM NaCl,
600 0.1% IGEPAL; B2: 20 mM HEPES, ph 7.5, 100 mM NaCl, 0.5% CHAPS; B3: 20 mM HEPES, pH 7.5, 250
601 mM Nacitrate, 0.5% CHAPS). Eventually, $2x10^8$ cells expressing Tb927.8.1950-V5 in addition to
602 TbPH1-BioID2-HA were lysed in B3 and processed as described below.

603 **Western blots**

604 Cell lysates were prepared by boiling in 1x SDS sample buffer and the equivalent of $2x10^6$ cells (RNAi
605 lines) or $4x10^6$ cells (IP samples) was loaded per well. Following western blotting, PVDF membranes
606 were blocked for 1 hour in 5% milk-PBS. Incubation with primary antibodies (anti-V5 at 1:1,000;
607 ThermoScientific, anti-HA at 1:1,000; ThermoScientific, anti-tubulin at 1:5,000; Sigma) was
608 performed at 4 °C overnight. Secondary antibodies (HRP-coupled anti-mouse or –rabbit IgG; Sigma)
609 were used at a concentration of 1:2,000 and signals were visualised using Clarity Western ECL
610 substrate (Bio-Rad) on a ChemiDoc MP (Bio-Rad).

611 **SYPRO Ruby staining**

612 Following electrophoresis, polyacrylamide gels were placed into fixing solution (7% glacial acetic
613 acid, 50% methanol) for 30 minutes at room temperature. Following another, identical fixation step,
614 the gel was incubated with SYPRO Ruby solution overnight at room temperature. A washing step in
615 washing solution (7% glacial acetic acid, 10% methanol) for 30 minutes at room temperature was
616 followed by three 5 minute washes in milliQ water before imaging on a ChemiDoc MP (Bio-Rad).

617 **Immunofluorescence and cytoskeleton extraction**

618 Approximately $2x10^6$ cells were used per slide. Cells were washed in PBS and fixed in 2.3% PFA in PBS
619 for approximately 30 minutes before being transferred to microscopy slides (ThermoScientific).
620 Following neutralisation in 0.1M glycine in PBS, slides were incubated in methanol at -20° C
621 overnight for permeabilisation. Slides were then rehydrated in PBS and blocked in 1% BSA in PBS for
622 1 hour followed by incubation with primary antibody for 1 hour in a humid chamber. The slides were
623 then washed three times with PBS before incubation in AlexaFluor-conjugated secondary antibody
624 (goat anti-rabbit/mouse, used at 1:1,000; Invitrogen). Following three further washes in PBS, a drop
625 of ProLong Gold Antifade reagent with DAPI (ThermoScientific) was added, a coverslip applied and
626 the slide sealed with nail polish. Slides were imaged with a Zeiss Axioscope or an Olympus FluoView
627 Fv1000 confocal microscope.

628 For immunofluorescence analysis of cells extracted using the 'MT sieving' fractionation method
629 described above the pellet fraction P2 was fixed in 2.3% PFA as described. All subsequent steps were
630 the same as for whole cell immunofluorescence.

631 To extract cytoskeletons conventionally, approximately 1x 10^7 PCF cells were collected and
632 centrifuged at room temperature for 5 min at 800 x g and the supernatant discarded. Thereafter, the
633 cell pellet was washed once in PBS and after resuspension in PBS applied in a drop-wise fashion to
634 Superfrost plus® slides (ThermoScientific). The cells were left to settle before the addition of PEME
635 buffer (100 mM Pipes, pH 6.9, 1 mM $MgSO_4$, 2 mM EGTA, 0.1 mM EDTA) containing 0.5% (v/v) NP-40
636 (Igepal) for 10 seconds. This cytoskeleton extraction was followed by a 10 minute fixation step in 4%
637 PFA. All subsequent steps were as described above for whole cell immunofluorescence.

638 Antibodies used in immunofluorescence

Antibody	Dilution	Origin
anti-HA (produced in rabbit)	1:1,000	Sigma, Catalog #: H6908
anti-V5 (produced in mouse)	1:1,000	ThermoScientific, Catalog #: 377500
1B41 (MtQ)[1]	1:1,000	(Gallo *et al.*, 1988)
L3B2	1:10	(Kohl *et al.*, 1999)
YL1/2	1:50	(Sherwin *et al.*, 1987)
GT335	1:2000	Adipogen Life Sciences, Catalog #: AG-20B-0020
[1]IgM purified from hybridoma supernatant and not mouse ascitic fluid as in original report.		

639

640 **Scanning and transmission electron microscopy**

641 For TEM, cell pellets were high-pressure frozen, freeze substituted in the presence of 2% OsO4 in
642 acetone, and embedded into Spi-Pon812 resin (SPI) as described previously (Kaurov *et al.*, 2018). For
643 SEM of the TbPH1/TbKifX2A RNAi cell line, cells were fixed in 2.5% glutaraldehyde in 100 mM PBS
644 overnight at 4°C and then spotted onto poly-l-lysine-coated glass cover slips. The cells were post-
645 fixed in 2% osmium tetroxide in 100 mM PBS for 1 h at room temperature and finally washed in the
646 same buffer. After dehydration cells were critical-point dried, coated with gold palladium and
647 imaged.

648 **Expansion microscopy**

649 Expansion microscopy samples were prepared as described previously (Gorilak *et al.*, 2021). In brief,
650 1x10^6 cells were fixed overnight in a solution containing 4% formaldehyde and 4% acrylamide in PBS
651 and adhered to a poly-L-lysine (Sigma, P4707) coated coverslip. The cells were gelated for 30 min at
652 37°C in PBS supplemented with 19% sodium acrylate, 10% acrylamide, and 0.1% N, N'-
653 Methylenebisacrylamide, 0.5% N, N, N´, N´-tetramethylethylenediamine, and 0.5% ammonium
654 persulfate. The specimens were further denatured by a 2 hour incubation at 95°C in a buffer
655 consisting of 50 mM tris(hydroxymethyl)aminomethane-hydrochloride, 200 mM sodium chloride,
656 200 mM sodium dodecyl sulphate, pH 9.0, and expanded by three 20 min incubations with 15 ml of
657 ultrapure water.

658 Thereafter, the gels were incubated overnight first with a mixture of anti-HA (Cell Signaling
659 Technology, 3724S; used at 1:250) and C3B9 ((Woods *et al.*, 1989), used at 1:10), anti-V5 (Sigma,
660 V8137-.2MG; used at 1:250) and C3B9 or anti-ClpGM6 ((Hayes *et al.*, 2014), used at 1:200) and C3B9
661 antibodies, followed by washes and an overnight incubation with a mixture of secondary antibodies
662 (Invitrogen, A11001 and A21428; used at 1:500). Both primary and secondary antibodies were
663 diluted in PBS supplemented with 2% bovine serum albumin. Finally, the gels were washed with
664 ultrapure water.

665 Prior to imaging pieces of gels containing stained expanded cells was transferred to a glass-bottom
666 dish coated with poly-L-lysine, and imaged using a Leica TCS SP8 confocal microscope with an HC PL
667 apochromatic 63x/NA 1.40 oil immersion objective. Z-stacks were acquired with the step size of 100
668 nm. Confocal z-stacks were processed in Fiji (Schindelin *et al.*, 2012). 3D reconstructions were
669 performed in the 3D viewer plugin.

670 **Flagellar pocket diameter measurements**

671 For FP diameter measurements, random DIC images were taken of TbPH1/TbKifX2A RNAi cells at
672 different time points and the diameter of 120 easily visible FPs measured in ImageJ (Rasband, W.S.,
673 ImageJ, U. S. National Institutes of Health, Bethesda, Maryland, USA, https://imagej.nih.gov/ij/,
674 1997-2018.).

675 **BioID**

676 PCF cells (TbPH1-BioID2-HA and SmOxP9 as controls) were grown in the presence of 50 µM biotin for
677 24 hours. For proximity-dependent biotin identification (BioID), 10^9 PCF cells were extracted in PEME
678 buffer (100 mM Pipes, pH 6.9, 1 mM $MgSO_4$, 2 mM EGTA, 0.1 mM EDTA) containing 0.5% (v/v) NP-40
679 (Igepal) for 15 minutes at room temperature resulting in extract E1. Following centrifugation at
680 3,400 x g for 2 minutes, supernatant S1 was created and pellet P1 was further processed by
681 extraction in lysis buffer (0.4% SDS, 500 mM NaCl, 5 mM EDTA, 1 mM DTT, 50 mM Tris-HCl, pH7.4).
682 Another centrifugation step at 16,000 x g for 10 minutes created supernatant S2. Both supernatants,
683 S1 and S2, were then incubated with streptavidin-conjugated Dynabeads (company) for 4 hours at 4
684 °C. An aliquot of flow through samples F1 and F2 were retained for western blotting and the
685 dynabeads were washed five times with PBS. A small sample of the beads was then resuspended in
686 2x SDS PAGE buffer and boiled, while the remainder of the beads was stored at -80 °C until further
687 processing for mass spectrometry analysis.

688 **Mass spectroscopy analysis of captured biotinylated proteins**

689 Trypsin-digestion of captured biotinylated proteins was performed on bead prior to liquid
690 chromatography-tandem mass spectroscopy (LC-MS/MS) as previously described (Pyrih *et al.*, 2020).
691 Data was processed using MaxQuant (Cox and Mann, 2008) version 1.6.14 which incorporates the
692 Andromeda search engine (Cox *et al.*, 2011). Proteins were identified by searching a protein
693 sequence database containing *T. brucei brucei* 927 annotated proteins (Version 51, TriTrypDB (Aslett
694 *et al.*, 2009), http://www.tritrypdb.org/) supplemented with frequently observed contaminants.
695 Carbamidomethylation of cysteine was set as a fixed modification and oxidation of methionine and
696 N-terminal protein acetylation were allowed as variable modifications. The experimental design
697 included matching between runs for biological replicates. Peptides were required to be at least 7
698 amino acids in length, with false discovery rates (FDRs) of 0.01 calculated at the levels of peptides,
699 proteins and modification sites based on the number of hits against the reversed sequence
700 database. The obtained data was subsequently processed in Perseus version 1.6.14 as described in
701 (Zoltner *et al.*, 2020).

702 **Mass spectroscopy analysis of whole cell lysates**

703 TbPH1/TbKifX2A RNAi cells were induced for 3 and 5 days with doxycycline, $5x10^7$ cells per replicate
704 collected by centrifugation and washed once in 1x PBS before being snap-frozen in liquid nitrogen.
705 Non-induced and parental control samples were also processed similarly as a control. MS LFQ
706 analysis was performed on biological triplicates. For sample prep, SP4 (Solvent Precipitation SP3)
707 protocol without beads was used (Harvey Johnston et al., 2021). Briefly, cell pellets (100 µg of

708 protein) were solubilized by SDS (final concentration 1% (w/v)), reduced with TCEP [tris(2-
709 carboxyethyl)phosphine], alkylated with MMTS (S-methyl methanethiosulfonate) and digested
710 sequentially with Lys-C and trypsin. Samples were desalted on Empore C18 columns, dried in a
711 speedvac and dissolved in 0.1% TFA + 2% acetonitrile. About 0.5 µg of peptide digests were
712 separated on a 50 cm C18 column using 60 min elution gradient and analyzed in DDA mode on an
713 Orbitrap Exploris 480 (Thermo Fisher Scientific) mass spectrometer.

714 Resulting raw files were analyzed in MaxQuant (v. 1.6.17.0) with label-free quantification (LFQ)
715 algorithm MaxLFQ and match between runs feature activated (Tyanova et al., 2016). FDR was set as
716 0.01 at all levels. TriTrypDB-56_TbruceiTREU927_AnnotatedProteins.fasta proteome file from
717 TriTrypDB (https://tritrypdb.org, Release 56) was used. MMTS alkylated cysteine was selected as a
718 fixed modification (Methylthio (C), composition: H(2) C S, +45.988). Variable modifications were
719 Oxidation (M) and Acetyl (Protein N-term). Downstream processing of the proteinGroups.txt file was
720 performed in Perseus v. 1.6.15.0. LFQ intensity values were log2 transformed and the rows were
721 filtered based on valid values (with a minimum of 2 in at least one group). The obtained data
722 (comparing TbPH1/TbKifX2A cells at T3 and T5 with T0) was additionally processed in Perseus
723 version 1.6.14 as described in (Zoltner et al., 2020).

724 **Bioinformatic analyses**

725 BLASTP search was performed in TriTrypDB using KIFX2A amino acid sequence as a search query,
726 returning hits with E=values <1e-20 . The 12 trypanosomatid predicted proteomes listed in Table S1A
727 was searched. These 12 proteomes were chosen based on their distribution within the consensus
728 trypanosomatid phylogenetic tree presented in Lukeš *et al.*(Lukeš *et al.*, 2018).

729 For constructing the kinesin phylogenetic tree depicted in Fig 7A, protein sequences that match the
730 Pfam 'kinesin motor domain' model (PF00225) from the same 12 predicted proteomes were mined
731 using HMMER v3.3 (Eddy, 2009). All sequences with an E-value <1e-40 (listed in Table S1C) were
732 taken for MAFFT alignment (Katoh *et al.*, 2002). Regions of the alignment that comprised of >50%
733 were removed. The phylogenetic tree based on the trimmed alignment was inferred with IQTree
734 v1.3.12 with JTT+F+G4 chosen as the best fit model according to BIC (Nguyen *et al.*, 2015). Branch
735 support was estimated using ultrafast bootstrap method. Tree was visualized using FigTree software
736 (http://tree.bio.ed.ac.uk/software/figtree/) and rooted arbitrarily.

737 **Data availability**

738 The mass spectrometry proteomics data have been deposited to the ProteomeXchange Consortium
739 via the PRIDE partner repository with the dataset identifiers PXD025802 (BioID) and PXD033717
740 (RNAi proteomes).

741 **ACKNOWLEDGEMENTS**

742 We thank Keith Gull (University of Oxford), Linda Kohl (Muséum National d'Histoire Naturelle), Bill
743 Wickstead (University of Nottingham), and Ziyin Li (University of Texas Medical School at Houston)
744 for helpful comments, Susanne Kramer (University of Würzburg), Cynthia He (National University of
745 Singapore), and Chris de Graffenried (Brown University) for antibodies, Peter Gorilak (Institute of
746 Molecular Genetics) for assistance with imaging and image analysis and Anzhelika Butenko (Biology
747 Centre, Czech Academy of Sciences) for advice on phylogenetic analysis. We acknowledge Karel
748 Harant and Pavel Talacko (BIOCEV, Prague) and Zbyněk Zdráhal and David Potěšil (CEITEC, Brno) and
749 the Proteomics Service Laboratory at the Institute of Physiology (supported by RVO, ID 67985823)
750 and Institute of Molecular Genetics (supported by RVO, ID 68378050) of the Czech Academy of

751 Sciences for mass spectroscopy analysis on BioID samples, excised bands and whole cell lysates,
752 respectively. This work was supported by the Czech Science Foundation grants 20-23513S to HH, and
753 21-09283S and ERC CZ LL1601 to JL, the ERD funds of the Czech Ministry of Education
754 16_019/0000759 to HH and JL, and BioImaging grant LM2018129 to MV. Work in the VV laboratory
755 was supported by an EMBO Installation Grant and by the J. E. Purkyne Fellowship of the Czech
756 Academy of Sciences.

757

758 **Author contributions**

759 Conceptualization (CB, NM, SK, VV, HH), formal analysis (CB, NM, SK, HV, MV, VV, HH), investigation
760 (CB, NM, SK, HV, MV), visualization (CB, VV, HH), writing – original draft (CB, HV, JL, VV, HH), funding
761 acquisition (JL, VV, HH), project administration (HH).

762

763 **Conflict of interest statement**

764 The authors declare that there's no conflict of interest.

765

766 **REFERENCES**

767 Albisetti, A., Florimond, C., Landrein, N., Vidilaseris, K., Eggenspieler, M., Lesigang, J., *et al.* (2017)
768 Interaction between the flagellar pocket collar and the hook complex via a novel microtubule-
769 binding protein in *Trypanosoma brucei*. *PLoS Pathog* **13**: e1006710

770 Alcantara, C. de L., Vidal, J.C., Souza, W. de, and Cunha-e-Silva, N.L. (2017) The cytostome-
771 cytopharynx complex of *Trypanosoma cruzi* epimastigotes disassembles during cell division. *J Cell Sci*
772 **130**: 164–176

773 Allingham, J.S., Sproul, L.R., Rayment, I., and Gilbert, S.P. (2007) Vik1 Modulates Microtubule-Kar3
774 Interactions through a Motor Domain that Lacks an Active Site. *Cell* **128**: 1161–1172

775 Amodeo, S., Kalichava, A., Fradera-Sola, A., Bertiaux-Lequoy, E., Guichard, P., Butter, F., and
776 Ochsenreiter, T. (2021) Characterization of the novel mitochondrial genome segregation factor
777 TAP110 in *Trypanosoma brucei*. *J Cell Sci* **134**: jcs.254300

778 An, T., and Li, Z. (2018) An orphan kinesin controls trypanosome morphology transitions by targeting
779 FLAM3 to the flagellum. *PLOS Pathog* **14**: e1007101

780 Aslett, M., Aurrecoechea, C., Berriman, M., Brestelli, J., Brunk, B.P., Carrington, M., *et al.* (2009)
781 TriTrypDB: A functional genomic resource for the Trypanosomatidae. *Nucleic Acids Res* **38**: D457–
782 D462

783 Benz, C., Stříbrná, E., Hashimi, H., and Lukeš, J. (2017) Dynamin-like proteins in *Trypanosoma brucei*:
784 A division of labour between two paralogs? *PLoS One* **12**: e0177200

785 Berriman, M., Ghedin, E., Hertz-Fowler, C., Blandin, G., Renauld, H., Bartholomeu, D.C., *et al.* (2005)
786 The genome of the African trypanosome *Trypanosoma brucei*. *Science* **309**: 416–422

787 Bertiaux, E., Mallet, A., Rotureau, B., and Bastin, P. (2020) Intraflagellar transport during assembly of
788 flagella of different length in *Trypanosoma brucei* isolated from tsetse flies. *J Cell Sci* **133**

789 Burkhard, P., Stetefeld, J., and Strelkov, S. V. (2001) Coiled coils: A highly versatile protein folding

790 motif. *Trends Cell Biol* **11**: 82–88

791 Cox, J., and Mann, M. (2008) MaxQuant enables high peptide identification rates, individualized
792 p.p.b.-range mass accuracies and proteome-wide protein quantification. *Nat Biotechnol* **26**: 1367–
793 1372

794 Cox, J., Neuhauser, N., Michalski, A., Scheltema, R.A., Olsen, J. V., and Mann, M. (2011) Andromeda:
795 A peptide search engine integrated into the MaxQuant environment. *J Proteome Res* **10**: 1794–1805

796 Darzynkiewicz, Z., Juan, G., and Bedner, E. (1999) Determining Cell Cycle Stages by Flow Cytometry.
797 *Curr Protoc Cell Biol* **1**: 8.4.1-8.4.18

798 Dean, S., Sunter, J., Wheeler, R.J., Hodkinson, I., Gluenz, E., and Gull, K. (2015) A toolkit enabling
799 efficient, scalable and reproducible gene tagging in trypanosomatids. *Open Biol* **5**: 140197.

800 Dean, S., Sunter, J.D., and Wheeler, R.J. (2017) TrypTag.org: A Trypanosome Genome-wide Protein
801 Localisation Resource. *Trends Parasitol* **33**: 80–82

802 Deltoro, D., Ortiz, D., Ordyan, M., Sippy, J., Oh, C.S., Keller, N., *et al.* (2016) Walker-A Motif Acts to
803 Coordinate ATP Hydrolysis with Motor Output in Viral DNA Packaging. *J Mol Biol* **428**: 2709–2729.

804 Dong, X., Lim, T.K., Lin, Q., and He, C.Y. (2020) Basal Body Protein TbSAF1 Is Required for
805 Microtubule Quartet Anchorage to the Basal Bodies in *Trypanosoma brucei*. *mBio* **11**: e00668-20

806 Eddy, S.R. (2009) A new generation of homology search tools based on probabilistic inference.
807 *Genome Inform* **23**: 205–211

808 El-Sayed, N.M., Myler, P.J., Bartholomeu, D.C., Nilsson, D., Aggarwal, G., Tran, A.N., *et al.* (2005) The
809 genome sequence of *Trypanosoma cruzi*, etiologic agent of Chagas disease. *Science* **309**: 409–415

810 Esson, H.J., Morriswood, B., Yavuz, S., Vidilaseris, K., Dong, G., and Warren, G. (2012) Morphology of
811 the trypanosome bilobe, a novel cytoskeletal structure. *Eukaryot Cell* **11**: 761–772.

812 Field, M.C., and Carrington, M. (2009) The trypanosome flagellar pocket. *Nat Rev Micro* **7**: 775–786

813 Field, M.C., Lumb, J.H., Adung'a, V.O., Jones, N.G., and Engstler, M. (2009) Chapter 1
814 Macromolecular Trafficking and Immune Evasion in African Trypanosomes. *Int Rev Cell Mol Biol* **278**:
815 1–67.

816 Fritz, M., Vanselow, J., Sauer, N., Lamer, S., Goos, C., Siegel, T.N., *et al.* (2015) Novel insights into RNP
817 granules by employing the trypanosome's microtubule skeleton as a molecular sieve. *Nucleic Acids*
818 *Res* **43**: 8013–8032

819 Gallo, J.M., and Precigout, E. (1988) Tubulin expression in trypanosomes. *Biol Cell* **64**: 137–143

820 Gallo, J.M., Précigout, E., and Schrével, J. (1988) Subcellular sequestration of an antigenically unique
821 beta-tubulin. *Cell Motil Cytoskeleton* **9**: 175–183

822 Gambarotto, D., Zwettler, F.U., Guennec, M. Le, Schmidt-Cernohorska, M., Fortun, D., Borgers, S., *et*
823 *al.* (2019) Imaging cellular ultrastructures using expansion microscopy (U-ExM). *Nat Methods* **16**: 71–
824 74

825 Gheiratmand, L., Brasseur, A., Zhou, Q., and He, C.Y. (2013) Biochemical characterization of the bi-
826 lobe reveals a continuous structural network linking the bi-lobe to other single-copied organelles in
827 *Trypanosoma brucei*. *J Biol Chem* **288**: 3489–3499

828 Gorilak, P., Pružincová, M., Vachova, H., Olšinová, M., and Varga, V. (2021) Expansion microscopy
829 facilitates quantitative super-resolution studies of cytoskeletal structures in kinetoplastid parasites.
830 *Open Biol* **11**: 210131

831 Gull, K. (1999) The cytoskeleton of trypanosomatid parasites. *Annu Rev Microbiol* **53**: 629–655

832 Hannaert, V., Albert, M.A., Rigden, D.J., Silva Giotto, M.T. Da, Thiemann, O., Garratt, R.C., *et al.*
833 (2003) Kinetic characterization, structure modelling studies and crystallization of *Trypanosoma*
834 *brucei* enolase. *Eur J Biochem* **270**: 3205–3213

835 Harvey Johnston, A.E., Yadav, K., Kirkpatrick, J.M., Biggs, G.S., Oxley, D., Kramer, H.B., et al. (2021)
836 Solvent Precipitation SP3 (SP4) enhances recovery for proteomics sample preparation without
837 magnetic beads. bioRxiv 2021.09.24.461247

838 Hayes, P., Varga, V., Olego-Fernandez, S., Sunter, J., Ginger, M.L., and Gull, K. (2014) Modulation of a
839 cytoskeletal calpain-like protein induces major transitions in trypanosome morphology. *J Cell Biol*
840 **206**: 377–384.

841 Hilton, N.A., Sladewski, T.E., Perry, J.A., Pataki, Z., Sinclair-Davis, A.N., Muniz, R.S., *et al.* (2018)
842 Identification of TOEFAZ1-interacting proteins reveals key regulators of *Trypanosoma brucei*
843 cytokinesis. *Mol Microbiol* **109**: 306–326

844 Hirokawa, N., and Noda, Y. (2008) Intracellular transport and kinesin superfamily proteins, KIFs:
845 Structure, function, and dynamics. *Physiol Rev* **88**: 1089–1118.

846 Hirokawa, N., Noda, Y., Tanaka, Y., and Niwa, S. (2009) Kinesin superfamily motor proteins and
847 intracellular transport. *Nat Rev Mol Cell Biol* **10**: 682–696

848 Hu, H., Hu, L., Yu, Z., Chasse, A.E., Chu, F., and Li, Z. (2012) An orphan kinesin in trypanosomes
849 cooperates with a kinetoplastid-specific kinesin to maintain cell morphology by regulating
850 subpellicular microtubules. *J Cell Sci* **125**: 4126–4136

851 Ivens, A.C., Peacock, C.S., Worthey, E.A., Murphy, L., Aggarwal, G., Berriman, M., *et al.* (2005) The
852 genome of the kinetoplastid parasite, *Leishmania major*. *Science* **309**: 436–442

853 Jentzsch, J., Sabri, A., Speckner, K., Lallinger-Kube, G., Weiss, M., and Ersfeld, K. (2020) Microtubule
854 polyglutamylation is important for regulating cytoskeletal architecture and motility in *Trypanosoma*
855 *brucei. J Cell Sci* **133**.

856 Katoh, K., Misawa, K., Kuma, K.I., and Miyata, T. (2002) MAFFT: a novel method for rapid multiple
857 sequence alignment based on fast Fourier transform. *Nucleic Acids Res* **30**: 3059–3066

858 Kaurov, I., Vancová, M., Schimanski, B., Cadena, L.R., Heller, J., Bílý, T., *et al.* (2018) The Diverged
859 Trypanosome MICOS Complex as a Hub for Mitochondrial Cristae Shaping and Protein Import. *Curr*
860 *Biol* **28**: 3393-3407.e5.

861 Kim, D.I., Birendra, K.C., Zhu, W., Motamedchaboki, K., Doye, V., and Roux, K.J. (2014) Probing
862 nuclear pore complex architecture with proximity-dependent biotinylation. *Proc Natl Acad Sci U S A*
863 **111**: 2453–2461.

864 Kim, D.I., Jensen, S.C., Noble, K.A., Kc, B., Roux, K.H., Motamedchaboki, K., and Roux, K.J. (2016) An
865 improved smaller biotin ligase for BioID proximity labeling. *Mol Biol Cell* **27**: 1188–1196.

866 Kohl, L., Sherwin, T., and Gull, K. (1999) Assembly of the paraflagellar rod and the flagellum
867 attachment zone complex during the *Trypanosoma brucei* cell cycle. *J Eukaryot Microbiol* **46**: 105–
868 109

869 Kramer, S., Queiroz, R., Ellis, L., Webb, H., Hoheisel, J.D., Clayton, C., and Carrington, M. (2008) Heat
870 shock causes a decrease in polysomes and the appearance of stress granules in trypanosomes
871 independently of eIF2α phosphorylation at Thr169. *J Cell Sci* **121**: 3002–3014

872 Lacomble, S., Vaughan, S., Gadelha, C., Morphew, M.K., Shaw, M.K., McIntosh, J.R., and Gull, K.

873 (2009) Three-dimensional cellular architecture of the flagellar pocket and associated cytoskeleton in
874 trypanosomes revealed by electron microscope tomography. *J Cell Sci* **122**: 1081–1090

875 Lacomble, S., Vaughan, S., Gadelha, C., Morphew, M.K., Shaw, M.K., McIntosh, J.R., and Gull, K.
876 (2010) Basal body movements orchestrate membrane organelle division and cell morphogenesis in
877 *Trypanosoma brucei*. *J Cell Sci* **123**: 2884–2891.

878 Li, Z., Lee, J.H., Chu, F., Burlingame, A.L., Günzl, A., and Wang, C.C. (2008) Identification of a Novel
879 Chromosomal Passenger Complex and Its Unique Localization during Cytokinesis in *Trypanosoma*
880 *brucei*. *PLoS One* **3**: e2354

881 Lott, K., Li, J., Fisk, J.C., Wang, H., Aletta, J.M., Qu, J., and Read, L.K. (2013) Global proteomic analysis
882 in trypanosomes reveals unique proteins and conserved cellular processes impacted by arginine
883 methylation. *J Proteomics* **91**: 210–225

884 Lukeš, J., Butenko, A., Hashimi, H., Maslov, D.A., Votýpka, J., and Yurchenko, V. (2018)
885 Trypanosomatids Are Much More than Just Trypanosomes: Clues from the Expanded Family Tree.
886 *Trends Parasitol* **34**: 466–480.

887 Marx, A., Hoenger, A., and Mandelkow, E. (2009) Structures of kinesin motor proteins. *Cell Motil*
888 *Cytoskeleton* **66**: 958–966

889 Morgan, G.W., Goulding, D., and Field, M.C. (2004) The single dynamin-like protein of *Trypanosoma*
890 *brucei* regulates mitochondrial division and is not required for endocytosis. *J Biol Chem* **279**: 10692–
891 701

892 Morriswood, B., Havlicek, K., Demmel, L., Yavuz, S., Sealey-Cardona, M., Vidilaseris, K., *et al.* (2013)
893 Novel bilobe components in *Trypanosoma brucei* identified using proximity-dependent biotinylation.
894 *Eukaryot Cell* **12**: 356–367.

895 Nguyen, L.T., Schmidt, H.A., Haeseler, A. Von, and Minh, B.Q. (2015) IQ-TREE: a fast and effective
896 stochastic algorithm for estimating maximum-likelihood phylogenies. *Mol Biol Evol* **32**: 268–274

897 Poon, S.K., Peacock, L., Gibson, W., Gull, K., and Kelly, S. (2012) A modular and optimized single
898 marker system for generating *Trypanosoma brucei* cell lines expressing T7 RNA polymerase and the
899 tetracycline repressor. *Open Biol* **2**: 110037

900 Pyrih, J., Rašková, V., Škodová-Sveráková, I., Pánek, T., and Lukeš, J. (2020) ZapE/Afg1 interacts with
901 Oxa1 and its depletion causes a multifaceted phenotype. *PLoS One* **15**: e0234918

902 Redmond, S., Vadivelu, J., and Field, M.C. (2003) RNAit: An automated web-based tool for the
903 selection of RNAi targets in *Trypanosoma brucei*. *Mol Biochem Parasitol* **128**: 115–118.

904 Robinson, D.R., Sherwin, T., Ploubidou, A., Byard, E.H., and Gull, K. (1995) Microtubule polarity and
905 dynamics in the control of organelle positioning, segregation, and cytokinesis in the trypanosome
906 cell cycle. *J Cell Biol* **128**: 1163–1172

907 Rotureau, B., Subota, I., and Bastin, P. (2011) Molecular bases of cytoskeleton plasticity during the
908 *Trypanosoma brucei* parasite cycle. *Cell Microbiol* **13**: 705–716.

909 Schindelin, J., Arganda-Carreras, I., Frise, E., Kaynig, V., Longair, M., Pietzsch, T., *et al.* (2012) Fiji: An
910 open-source platform for biological-image analysis. *Nat Methods* **9**: 676–682

911 Sherwin, T., Schneider, A., Sasse, R., Seebeck, T., and Gull, K. (1987) Distinct localization and cell
912 cycle dependence of COOH terminally tyrosinolated α-tubulin in the microtubules of *Trypanosoma*
913 *brucei brucei*. *J Cell Biol* **104**: 439–446

914 Sinclair, A.N., and Graffenried, C.L. de (2019) More than Microtubules: The Structure and Function of

915 the Subpellicular Array in Trypanosomatids. *Trends Parasitol* **35**: 760–777

916 Skalický, T., Dobáková, E., Wheeler, R.J., Tesařová, M., Flegontov, P., Jirsová, D., *et al.* (2017)
917 Extensive flagellar remodeling during the complex life cycle of Paratrypanosoma, an early-branching
918 trypanosomatid. *Proc Natl Acad Sci U S A* **114**: 11757–11762.

919 Sunter, J.D., and Gull, K. (2016) The Flagellum Attachment Zone: 'The Cellular Ruler' of Trypanosome
920 Morphology. *Trends Parasitol* **32**: 309–324 https://pubmed.ncbi.nlm.nih.gov/26776656/. Accessed
921 December 14, 2020.

922 Tinti, M., Ferguson, M.A.J., Yurchenko, V., and Magez, S. (2022) Visualisation of proteome-wide
923 ordered protein abundances in *Trypanosoma brucei*. *Wellcome Open Res 2022 734* **7**: 34

924 Tyanova, S., Temu, T., and Cox, J. (2016) The MaxQuant computational platform for mass
925 spectrometry-based shotgun proteomics. Nat Protoc 2016 1112 11: 2301–2319

926 Urbaniak, M.D., Guther, M.L.S., and Ferguson, M. a J. (2012) Comparative SILAC proteomic analysis
927 of *Trypanosoma brucei* bloodstream and procyclic lifecycle stages. *PLoS One* **7**: e36619

928 Varga, V., Moreira-Leite, F., Portman, N., and Gull, K. (2017) Protein diversity in discrete structures at
929 the distal tip of the trypanosome flagellum. *Proc Natl Acad Sci U S A* **114**: E6546–E6555

930 Wei, Y., Hu, H., Lun, Z.-R., and Li, Z. (2013) The Cooperative Roles of Two Kinetoplastid-Specific
931 Kinesins in Cytokinesis and in Maintaining Cell Morphology in Bloodstream Trypanosomes. *PLoS One*
932 **8**: e73869

933 Wheeler, R.J., Gull, K., and Sunter, J.D. (2019) Coordination of the cell cycle in trypanosomes. *Annu*
934 *Rev Microbiol* **73**: 133–154

935 Wheeler, R.J., Scheumann, N., Wickstead, B., Gull, K., and Vaughan, S. (2013) Cytokinesis in
936 *Trypanosoma brucei* differs between bloodstream and tsetse trypomastigote forms: implications for
937 microtubule-based morphogenesis and mutant analysis. *Mol Microbiol* **90**: 1339–1355

938 Wickstead, B., Carrington, J.T., Gluenz, E., and Gull, K. (2010a) The expanded kinesin-13 repertoire of
939 trypanosomes contains only one mitotic kinesin indicating multiple extra-nuclear roles. *PLoS One* **5**:
940 e0015020

941 Wickstead, B., Ersfeld, K., and Gull, K. (2002) Targeting of a tetracycline-inducible expression system
942 to the transcriptionally silent minichromosomes of *Trypanosoma brucei*. *Mol Biochem Parasitol* **125**:
943 211–6

944 Wickstead, B., and Gull, K. (2006) A "Holistic" Kinesin Phylogeny Reveals New Kinesin Families and
945 Predicts Protein Functions. *Mol Biol Cell* **17**: 1734–1743.

946 Wickstead, B., Gull, K., and Richards, T.A. (2010b) Patterns of kinesin evolution reveal a complex
947 ancestral eukaryote with a multifunctional cytoskeleton. *BMC Evol Biol* **10**:

948 Woods, A., Sherwin, T., Sasse, R., MacRae, T.H., Baines, A.J., and Gull, K. (1989) Definition of
949 individual components within the cytoskeleton of *Trypanosoma brucei* by a library of monoclonal
950 antibodies. *J Cell Sci* **93 (Pt 3)**: 491—500

951 Woodward, R., and Gull, K. (1990) Timing of nuclear and kinetoplast DNA replication and early
952 morphological events in the cell cycle of *Trypanosoma brucei*. *J Cell Sci* **95 (Pt 1)**: 49–57

953 Zhou, Q., An, T., Pham, K.T.M., Hu, H., and Li, Z. (2018) The CIF1 protein is a master orchestrator of
954 trypanosome cytokinesis that recruits several cytokinesis regulators to the cytokinesis initiation site.
955 *J Biol Chem* **293**: 16177–16192

956 Zoltner, M., Pino, R.C. del, and Field, M.C. (2020) Sorting the Muck from the Brass: Analysis of
957 Protein Complexes and Cell Lysates. In *Methods in Molecular Biology*. Humana Press Inc., pp. 645–
958 653

959

960 **FIGURE LEGENDS**

961 **Fig. 1:** Domain architecture of TbPH1 and TbKifX2A **(A)** and TbKifX2C **(B)**. Schematic depiction
962 includes phosphorylation and arginine methylation sites. The consensus Walker A motif is shown in
963 between the two schemata in A for comparison of the respective motifs within the kinesin motor
964 domains of TbPH1 and TbKifX2A. Key residues in ATP hydrolysis shown in red and mutations in
965 purple. The likely inactive state of the TbPH1 'kinesin motor domain' is highlighted by striped
966 pattern. CC: coiled coil domain, PH: pleckstrin homology domain, HDL: homeodomain-like fold.

967 **Fig. 2:** TbPH1-V5 fractionates with the cytoskeleton. **(A)** Western blot of-trypanosome cell fractions
968 with equal cell equivalents loaded per lane as previously described in (Fritz *et al.*, 2015).
969 Fractionation procedure is summarized in S1 Fig. Antibodies used were anti-V5 and anti-SCD6
970 (Kramer *et al.*, 2008). T: total lysate, SN: supernatant, P: pellet. **(B)** IFA of on an aliquot of fraction P2
971 placed on microscope slide. Cells were labelled with anti-V5 antibody (green) and DAPI (blue). The
972 scale bar corresponds to 5 µm.

973 **Fig. 3:** TbPH1 interacts with TbKifX2A, a kinetoplastid-specific kinesin. **(A)** Western blot verifying
974 immunoprecipitation of TbPH1-V5. The blot was probed with anti-V5 and anti-α-tubulin antibodies.
975 The parental cell line SmOxP9 was used as a control. T: total lysate, SN3: supernatant 3, FT: flow
976 through, E: elution. **(B)** SyproRuby-stained gel of elution fractions of TbPH1-V5 IP and mock control
977 (SmOxP9). B1 and B2: bands excised and by mass spectrometry identified to be TbPH1 and TbKifX2A,
978 respectively. Asterisks: band corresponding to denatured immunoglobulin light chain that was
979 incidentally eluted. **(C)** Western blot showing interaction of TbPH1-V5 and TbKifX2A-HA. TbKifX2A-
980 HA was immunoprecipitated in the same way as PH1-V5. Lanes loaded as in Fig. 2A. T: total lysate,
981 SN: supernatant, P: pellet, FT: flow through, E: elution. **(D)** IFA on whole cells detecting TbPH1-V5
982 (white) and counterstained with DAPI to visualize DNA (magenta). Arrowheads denote increased
983 signal in the area along the proximal part of the flagellum. Asterisks demark an increased signal at
984 the anterior cell body end. Merge of DAPI and Phase contrast images shown on bottom. Scale bar,
985 10 µm. **(E)** IFA on whole cells detecting TbKifX2A-HA (white). Images depicted as in **D**. **(F)** IFA on
986 whole cells detecting TbPH1-V5 (green) and TbKifX2A (magenta). The merged image is also
987 counterstained with DAPI (blue) to visualize DNA. Scale bar, 5 µm. Close up views of parts with
988 strongest signals (white boxes) also shown. Scale bar, 1 µm

989 **Fig. 4:** Localization of cytoskeleton-associated TbKifX2A and TbPH1. **(A)** IFA on extracted
990 cytoskeletons probing localisation of TbPH1-V5 (green) and TbKifX2A-HA (magenta). **(B)** IFA on
991 extracted cytoskeletons probing co-localisation of TbKifX2A-HA (magenta) with the FAZ (green), the
992 latter labelled with L3B2 antibody. **(C)** IFA on extracted cytoskeletons probing co-localisation of
993 TbKifX2A-HA (magenta) with basal bodies (green), the latter labelled with YL1/2 antibody **(D)** IFA on
994 extracted cytoskeletons probing co-localisation of TbKifX2A-HA (magenta) with the MtQ (green), the
995 latter labelled with 1B41 antibody. In all panels, merge images depict co-localization in white and
996 DIC on right showing observed extracted cytoskeleton. Scale bar, 5 µm. Close up views of parts with
997 strongest signals (white boxes) shown in rightmost images. Scale bar, 1 µm.

998 **Fig 5:** TbKifX2A and TbPH1 localize to the MtQ. Ultrastructure expansion microscopy images
999 depicted as 3D projections (A-D) and representative confocal image sections used to make

1000 projections (E-F) of *T. brucei* expressing TbPH1-V5 and TbKifX2A-HA. (A) 3D reconstruction of the
1001 area of the cell in the vicinity of the basal body and flagellum exit from the flagellar pocket looking
1002 from outside the MT corset. Top shows signal of anti-V5 (green) and anti-acetylated α-tubulin
1003 (white) antibodies. Bottom is the same image of anti-acetylated α-tubulin signal only with relevant
1004 structures marked. Tick marks at 5 µm increments (A-C). (B) Similar reconstruction as in A but of a
1005 cell with two flagella, showing anti-HA antibody signal (green) and a view shown from inside the MT
1006 corset. (C) 3D reconstruction of the posterior part of the cell. Signal colors correspond to A. (D) 3D
1007 reconstruction of whole dividing *T. brucei* cell. Signal colors correspond to B. Box highlights region of
1008 interest shown in F. Tick marks at 10 µm increments. (E) Confocal images of a single plane from the
1009 vicinity of the basal body showing from left to right signal of anti-V5 and anti-acetylated α-tubulin
1010 antibodies(both white) plus an overlay of both signals with V5 signal in green. Left image shows 5
1011 µm scale bar. Middle image marks relevant structures. (F) Same as in E except two confocal planes
1012 being shown, focusing on new (Top) and old MtQ (Bottom), and the left images showing anti-HA
1013 antibody signal. Solid arrowheads point to overlay of epitope antibody signal and MtQ. Hollow
1014 arrowheads point to representative epitope antibody signals found in the cytosol.

1015 **Fig. 6:** The proximal proteome of TbPH1. **(A)** IFA on whole cells showing localisation of TbPH1-
1016 BioID2-HA (green) and biotinylated proteins (magenta) and counterstained with DAPI (blue).
1017 Arrowheads denote signal in vicinity of kinetoplast, near the proximal part of the flagellum. DIC on
1018 right to show observed cell. Scale bar, 5 µm. **(B)** IFA as in **A** of parental cell line lacking TbPH1-BioID2-
1019 HA. **(C)** Western blot (top panel) and fluorescently-detected proteins resolved on SDS-PAGE as a
1020 loading control (bottom panel, stain-free gel) of a representative BioID experiment. The blot was
1021 probed with anti-HA to confirm the presence of TbPH1-BioID2-HA in the respective fractions. E:
1022 extract, P: pellet, S: supernatant, F: flow through, B: boiled beads. **(D)** Volcano plot with -10 log t-test
1023 p value plotted against the t-test difference between TbPH1-BioID2-HA sample and mock (SmOxP9
1024 cells) from three biological replicates. Statistically significant hits are found above the curve in the
1025 top right quadrant and their identity is indicated. Accession numbers are given with additional
1026 annotations in parentheses; these are color coded based on their localization determined by TrypTag
1027 (Dean *et al.*, 2017). **(E)** Heat map of SAINTq score (*i.e.* P value) of proteins interacting with TOEFAZ1
1028 (Hilton *et al.*, 2018), the relative enrichment of proteins also found in the TbPH1 proximal proteome
1029 are indicated. a:Tb927.3.2490 (TbPH1), b: Tb927.8.1950 (ApbE-like domain), c: Tb927.9.15470
1030 (TbKifX2A), d: Tb927.3.4720/60 (DLP1/2). PG, protein groups. **(F)** Western blot showing interaction
1031 between FP45-V5/kinesin Tb927.6.2880-V5 (TbKifX2C) and TbPH1-BioID2-HA. S: supernatant, F: flow
1032 through, B: boiled beads. Black arrowhead pointing to anti-HA and white arrowhead pointing to anti-
1033 V5 signals. **(G)** Venn diagram comparing the proximity proteome of TbPH1 with those of the TOEFAZ
1034 (as depicted in **E**), the hook complex protein TbMORN1 (all 79 biotinylated proteins (Morriswood *et*
1035 *al.*, 2013)), and the 11 high confidence proteins in the TbSpef1, a MtQ binding protein (Dong *et al.*,
1036 2020). Proteins exclusive to the TbPH1 proximity proteome are highlighted in green while magenta
1037 highlights those that are found to also be in proximity with TOEFAZ.

1038 **Fig. 7:** TbKifX2C is part of the X2 clade of kinesins and partially co-localizes with TbPH1. **(A)**
1039 Phylogenetic tree of 549 trypanosomatid sequences matching the 'kinesin motor domain' model
1040 with high confidence (see Materials and Methods). Clades containing sequences that lie outside of
1041 the X2 family were collapsed and named based on the presence of *L. major* and/or *T. brucei*
1042 representatives belonging to kinesin families as defined by Wickstead and colleagues (Wickstead and
1043 Gull, 2006; Wickstead *et al.*, 2010b). The numbers of sequences belonging to each clade is shown
1044 within each triangle that is also shaded based on the number of contained sequences. Branch
1045 support values >50 are depicted; those values >95 and 100 are marked by closed and open circles,
1046 respectively. Four pointed star marks X2 family sequences as annotated by Wickstead and co-

1047 workers. Scale bar, number of substitutions per site. **(B)** IFA on whole cells (top two rows) and
1048 extracted cytoskeletons (bottom row) probing co-localisation of TbKifX2C-V5 (green) with TbPH1-
1049 BioID2-HA (magenta). Scale bar, 5 µm. Close up views of parts of strongest signal (white boxes) also
1050 shown. Scale bar, 1 µm. **(C)** Tukey plot showing differential expression of *T. brucei* X2 family kinesins
1051 in long slender bloodstream (B) and procylic (P) stages based on LC-MS/MS iBAQ values from Tinti
1052 and Ferguson (Tinti *et al.*, 2022) depicted on logarithmic scale on *y*-axis. Numbers above x-*axis*
1053 report number of iBAQ spectra per sample. Colored numbers below each boxplot denote the median
1054 iBAQ value. ****, P<0.0001; *, P<0.05.

1055 Fig. 8: TbPH1/TbKifX2A RNAi. **(A)** Growth curves of single TbPH1 and TbKifX2A RNAi cell lines. Filled
1056 circles: TbKifX2A – tet, open circles: TbKifX2A + tet, filled triangles: TbPH1 – tet, open triangles:
1057 TbPH1 + tet. Standard deviation of measurements at each time point (n=3) is not visible at this scale.
1058 Insets show western blots probed with anti-HA (to detect TbKifX2A), anti-V5 (to detect TbPH1) and
1059 anti-α-tubulin as a loading control. **(B)** Growth curve of double TbPH1/TbKifX2A RNAi cell line. Filled
1060 circles: TbPH1/TbKifX2A – tet, open circles: TbPH1/TbKifX2A + tet. Standard deviation of
1061 measurements at each time point (n=3) is not visible at this scale. Inset depicts western blot showing
1062 depletion of TbPH1/TbKifX2A. Samples were taken at the same time as the growth curve in B was
1063 performed. The blot was probed with anti-HA (to detect TbKifX2A), anti-V5 (to detect TbPH1) and
1064 anti-α-tubulin as a loading control. **(C)** Bar chart depicting proportions of cells in different cell cycle
1065 phases during TbPH1/TbKifX2A RNAi time course. DAPI counts were performed in triplicate with at
1066 least 200 cells counted per time point. N: nucleus, K: kinetoplast. **(D)** Flow cytometry analysis of
1067 different cell cycle phases during TbPH1/TbKifX2A RNAi time course. Analyses were performed in
1068 triplicate and standard deviation is shown with error bars. Statistically significant increases in
1069 number of zoid formation compared to time point 0 is shown to the left of relevant (light blue stars;
1070 **, P<0.01; ***, P<0.001).

1071 Fig. 9: Effects of TbPH1/TbKifX2A RNAi. **(A)** Volcano plots with -10 log t-test p value plotted against
1072 the t-test difference between TbPH1/TbKifX2A RNAi sample induced for 3 (T3) and 5 (T5) days,
1073 respectively, and mock (non-induced control) from three biological replicates. Statistically significant
1074 hits are found above the curve in both top right and left quadrants and their identity is indicated. **(B)**
1075 Depletion of TbPH1/TbKifX2A causes an increase in flagellar pocket diameter. Left: Example DIC
1076 images of TbPH1/TbKifX2A RNAi cells (T0 and T5), arrows pointing at flagellar pockets. Right**:** Scatter
1077 plot depicting flagellar pocket diameters from 120 cells per time point. Longer middle line
1078 corresponds to the mean and whiskers are the standard deviation. Light grey circles: T0, medium
1079 grey squares: T3, dark grey triangles: T5. **(C)** Scanning electron microscopy of TbPH1/TbKifX2A RNAi
1080 cells. T0: non-induced; T5: 5 day RNAi induction. Arrows pointing to posterior end protrusions. The
1081 scale bar corresponds to 10 µm. Quantification of 'glove' phenotype from >380 cells per time point
1082 shown.

1083

1084 **S1 Fig.:** Schematic depiction of microtubule sieving technique. According to (Fritz *et al.*, 2015).

1085 **S2 Fig.:** Wider field of view of multiple extracted cytoskeletons co-localizing TbKifX2A and TbPH1 to
1086 basal body **(C)**, FAZ **(D)** and MtQ **(E)**. Images depicted as in Fig 4 with scale bar corresponding to 5
1087 µm. **(A)** Co-localization (merge, white) of TbPH1-V5 (green) and TbKifX2A-HA (magenta). **(B)** Parental
1088 cell line lacking TbPH1-V5 and TbKifX2A-HA, incubated with antibodies recognizing V5 and HA
1089 epitopes used to acquire other IFA images.

1090 **S3 Fig.:** Ultrastructure expansion microscopy of a cell labelled with anti-ClpGM6 (to detect the FAZ,
1091 green) and anti-acetylated α tubulin antibody C3B9 (grey). Only the region around the flagellar
1092 pocket and flagellum exit shown. Similar region of a cell stained for TbPH1-V5 from Fig. 5A shown for
1093 comparison. The areas are shown under different angles. Arrowheads indicate the part of the MtQ
1094 inside the corset.

1095 **S4 Fig.:** Schematic depiction of proximity-dependent biotinylation (BioID). According to (Morriswood
1096 *et al.*, 2013). Only steps in black were performed in our study.

1097 **S5 Fig.:** Tb927.8.1950-V5. **(A)** Western blot showing size difference between Tb927.8.1950-V5 in
1098 whole cell lysates (WCL) and BioID S1 fraction (S1). **(B)** Western blot showing size and solubility in
1099 different lysis buffers. S: soluble, P: pellet, B1: 10 mM Tris-Cl, pH7.8, 150 mM NaCl, 0.1% IGEPAL; B2:
1100 20 mM HEPES, ph 7.5, 100 mM NaCl, 0.5% CHAPS; B3: 20 mM HEPES, pH 7.5, 250 mM Nacitrate,
1101 0.5% CHAPS. **(C)** Western blot showing IP of Tb927.8.1950-V5. The blot was also probed for the
1102 presence of TbPH1-BioID-HA. S: supernatant, F: flow through, B: boiled beads.

1103 **S6 Fig.: (A)** Bar chart showing population doubling times for TbPH1, KifX2A and TbPH1/KifX2A
1104 depletion cell lines. -/+: -/+ doxycycline to induce RNAi, the average difference in hours from three
1105 experiments is shown above the respective bars. Standard deviation shown using whiskers. **(B)** IFA of
1106 TbPH1/TbKifX2A RNAi cells. T0: non-induced, T5: induced for 5 days. Extracted cytoskeletons were
1107 labelled with L3B2 (recognising the FAZ filament, green), mAB 1B41 (recognising the MtQ, magenta)
1108 and DAPI (blue). Scale bar, 5 µm. (C) Flow cytometry histograms of TbPH1/TbKifX2A RNAi cells. Three
1109 replicates are shown, asterisk marks the appearing zoid peak in one example histogram.

1110 **S7 Fig.:** Transmission electron microscopy and IFA of TbPH1/TbKifX2A RNAi cell line. Cells were
1111 induced for 5 days. **(A)** TEM image depicting posterior end protrusions (arrow). Scale bar, 1 µm. **(B)**
1112 Top: IFA on cytoskeletons probing effects of TbPH1/TbKifX2A depletion on post-translational
1113 modifications of tubulin. Cells were stained with GT335 (white, staining glutamyl side chains). The
1114 scale bar corresponds to 5 µm. Bottom: Western blot of cells taken after 3 to 5 days of growth in
1115 presence (T3, T5) or absence (T0) of doxycycline probed with antibodies recognizing GT335 and α-
1116 enolase (Hannaert *et al.*, 2003), the latter used as a loading control.

1117 **Table S1:** Bioinformatic analysis of X2 family kinesins. **(A)** List of predicted trypanosomatid
1118 proteomes used in this study with the protein name prefixes used to name utilized sequences. **(B)**
1119 List of proteins retuned by BLASTP with E-value<1e-20 by searching the predicted trypanosomatid
1120 proteomes with TbKifX2A query sequence. **(C)** List of 549 trypansomatid sequences that match the
1121 'kinesin motor domain' model (Pfam PF00225) with E-vale<1e-40 by HMMER search (Eddy, 2009).

1122 **S1 Dataset:** Mass spectrometry analysis of excised bands B1 and B2 from Fig. 3B.

1123 **S2 Dataset:** Mass spectrometry data of TbPH1 BioID experiment. Data with and without imputation
1124 and filtered for Andromeda scores >20 and presence of >1 unique peptide, which was used to
1125 generate the volcano plot in Fig. 6D.

1126 **S3 Dataset:** Mass spectrometry data of whole cell lysate TbPH1/TbKifX2A RNAi experiment. Data
1127 filtered for Andromeda scores >10 and presence of >1 unique peptide, which was used to
1128 generate the volcano plots in Fig. 9A.

1129

1130

1131

Fig. 1

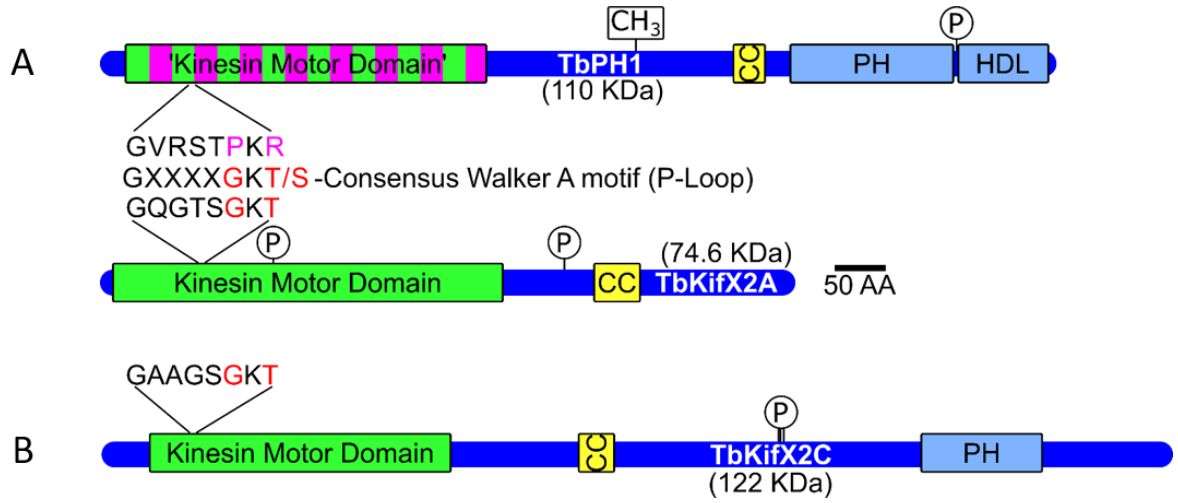
A
'Kinesin Motor Domain'
CH3
TbPH1
(110 KDa)
CC
PH
P
HDL
GVRSTPKR
GXXXXGKT/S -Consensus Walker A motif (P-Loop)
GQGTSGKT
P
Kinesin Motor Domain
P
CC
(74.6 KDa)
TbKifX2A
50 AA
GAAGSGKT
B
Kinesin Motor Domain
CC
P
TbKifX2C
(122 KDa)
PH

Fig. 2

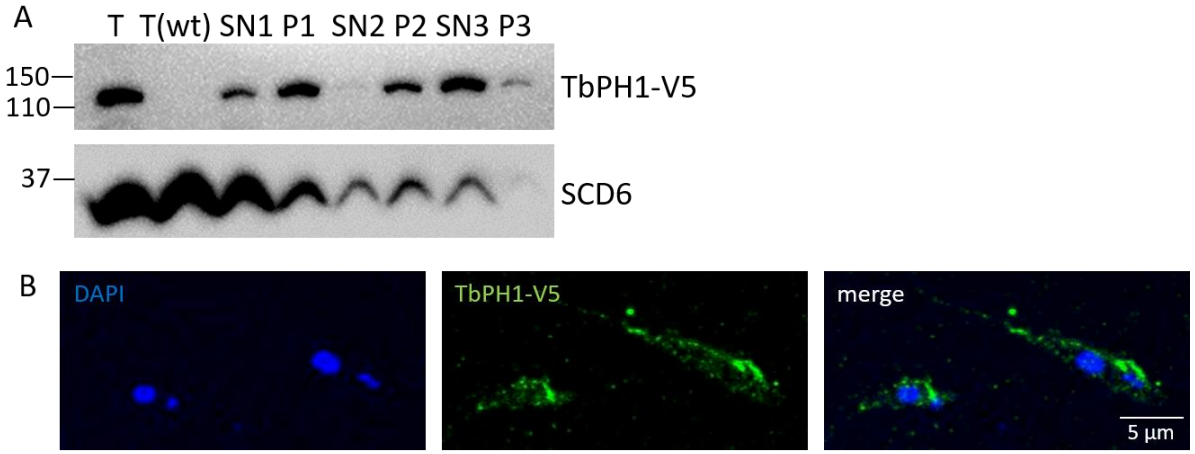
A
T T(wt) SN1 P1 SN2 P2 SN3 P3
150
110
TbPH1-V5
37
SCD6
B
DAPI
TbPH1-V5
merge
5 µm

Fig. 3

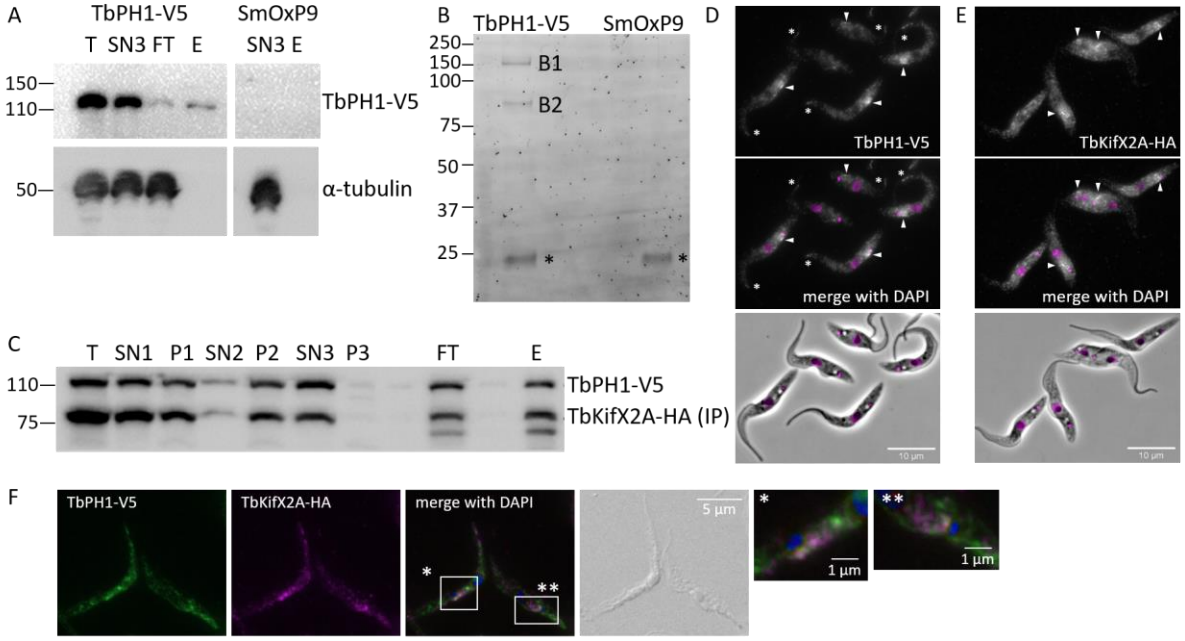
A
TbPH1-V5
SmOxP9
T SN3 FT E
SN3 E
150
110
50
TbPH1-V5
α-tubulin
B
TbPH1-V5
SmOxP9
250
150
100
75
50
37
25
B1
B2
C
T SN1 P1 SN2 P2 SN3 P3 FT E
110
75
TbPH1-V5
TbKifX2A-HA (IP)
D
TbPH1-V5
merge with DAPI
E
TbKifX2A-HA
merge with DAPI
F
TbPH1-V5
TbKifX2A-HA
merge with DAPI
5 µm
1 µm
1 µm

Fig. 4

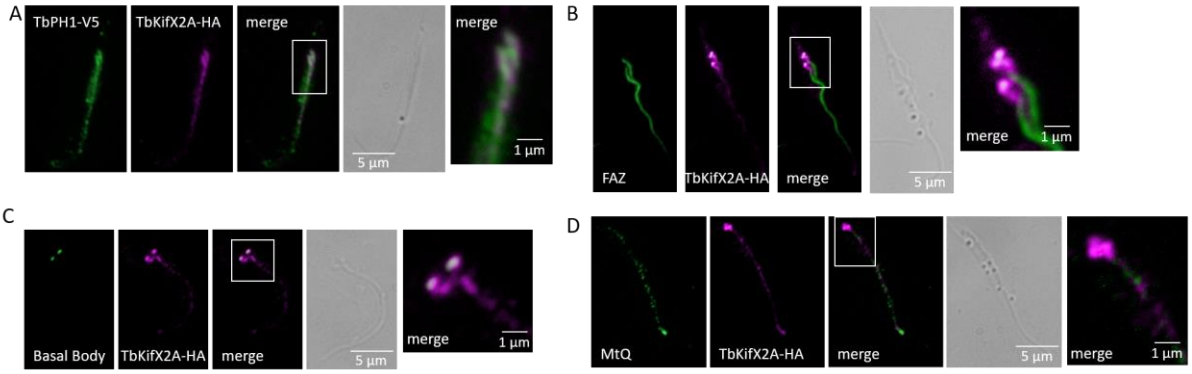
A
TbPH1-V5
TbKifX2A-HA
merge
5 µm
merge
1 µm
B
FAZ
TbKifX2A-HA
merge
5 µm
merge
1 µm
C
Basal Body
TbKifX2A-HA
merge
5 µm
merge
1 µm
D
MtQ
TbKifX2A-HA
merge
5 µm
merge
1 µm

Fig. 5

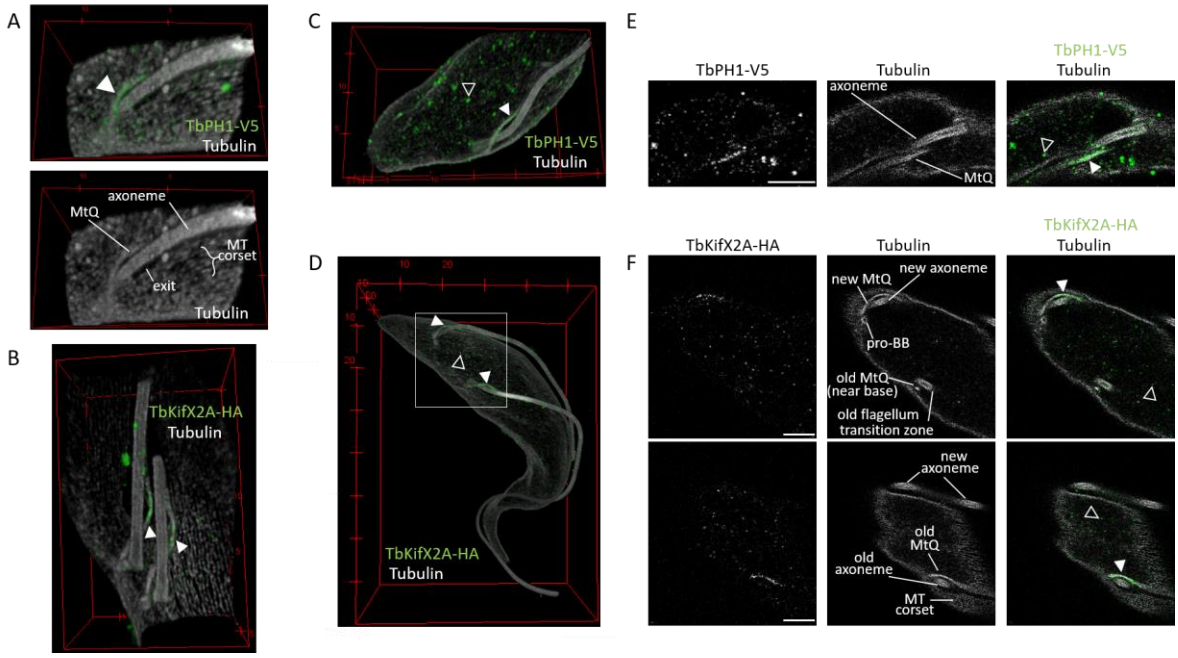
A
TbPH1-V5
Tubulin
axoneme
MtQ
MT corset
exit
Tubulin
B
TbKifX2A-HA
Tubulin
C
TbPH1-V5
Tubulin
D
TbKifX2A-HA
Tubulin
E
TbPH1-V5
Tubulin
axoneme
MtQ
TbPH1-V5
Tubulin
F
TbKifX2A-HA
Tubulin
new MtQ
new axoneme
pro-BB
old MtQ (near base)
old flagellum transition zone
TbKifX2A-HA
Tubulin
new axoneme
old MtQ
old axoneme
MT corset

Fig. 6

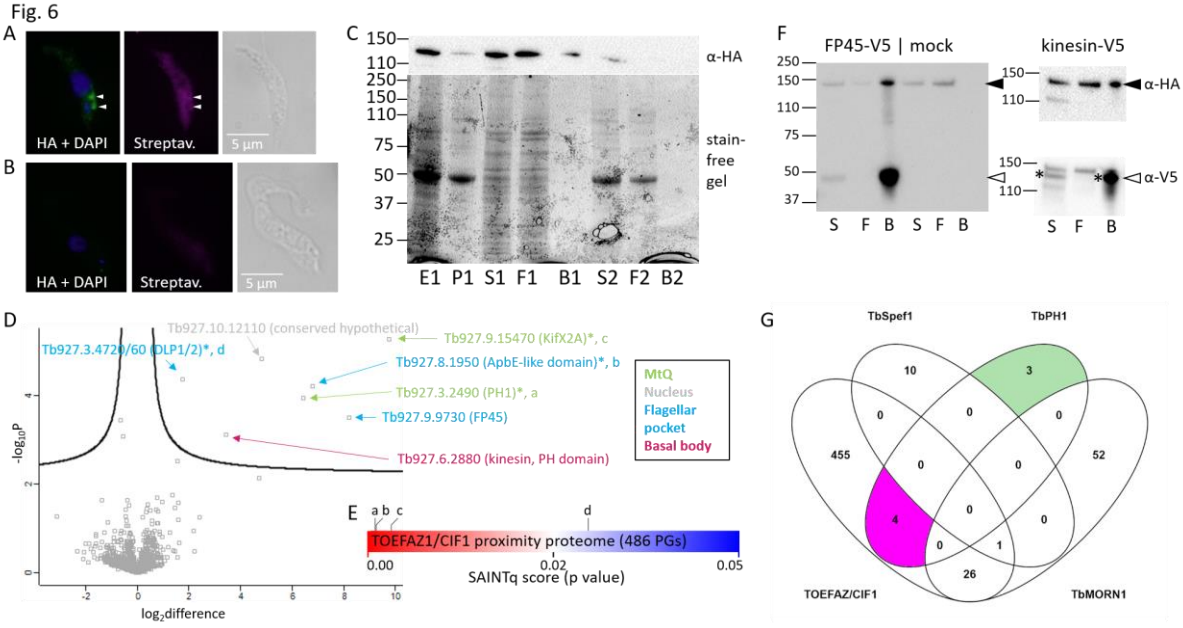
A
HA + DAPI
Streptav.
5 µm
B
HA + DAPI
Streptav.
5 µm
C
150
110
250
150
110
75
50
37
25
α-HA
stain-free gel
E1 P1 S1 F1 B1 S2 F2 B2
D
Tb927.10.12110 (conserved hypothetical)
Tb927.3.4720/60 (DLP1/2)*, d
Tb927.9.15470 (KifX2A)*, c
Tb927.8.1950 (ApbE-like domain)*, b
Tb927.3.2490 (PH1)*, a
Tb927.9.9730 (FP45)
Tb927.6.2880 (kinesin, PH domain)
MtQ
Nucleus
Flagellar pocket
Basal body
-log10P
log2difference
E
a b c
d
TOEFAZ1/CIF1 proximity proteome (486 PGs)
0.00
0.02
0.05
SAINTq score (p value)
F
FP45-V5 | mock
kinesin-V5
250
150
110
75
50
37
S F B S F B
α-HA
α-V5
S F B
G
TbSpef1
TbPH1
TOEFAZ/CIF1
TbMORN1
10
3
0
0
0
455
0
0
52
4
0
0
0
1
26

Fig. 7

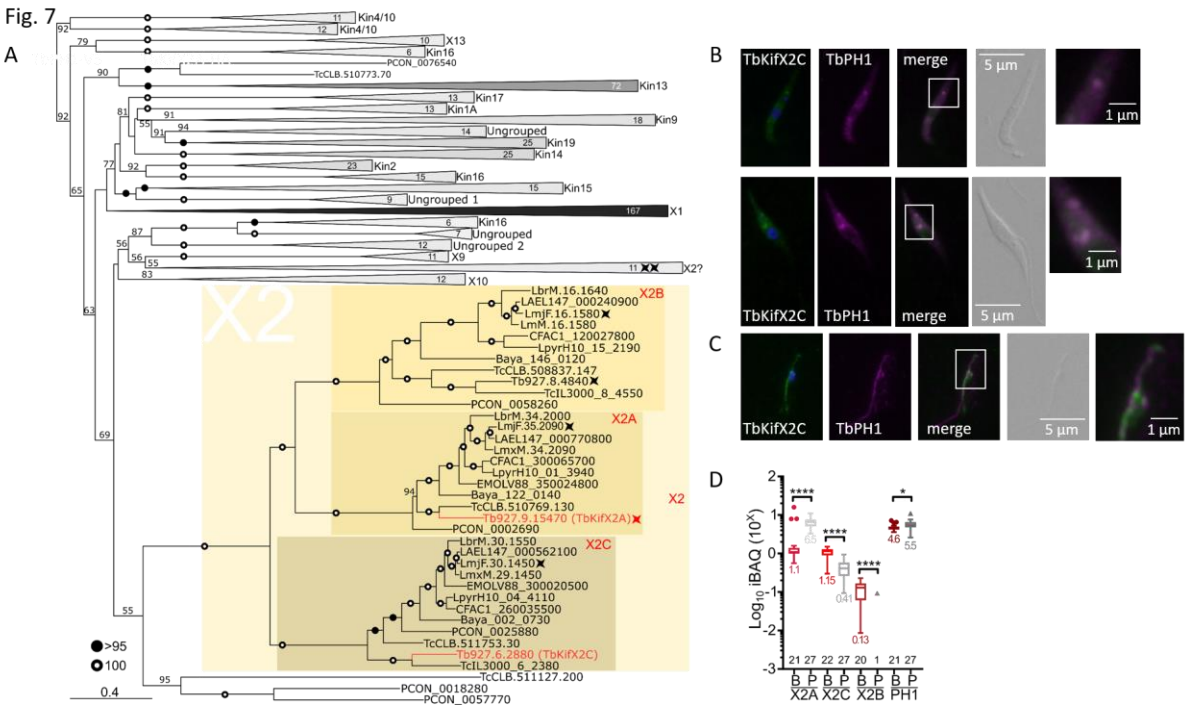

1269
1270
1271
1272
1273
1274
1275
1276
1277
1278
1279
1280
1281
1282
1283
1284
1285
1286
1287
1288
1289

Fig. 8

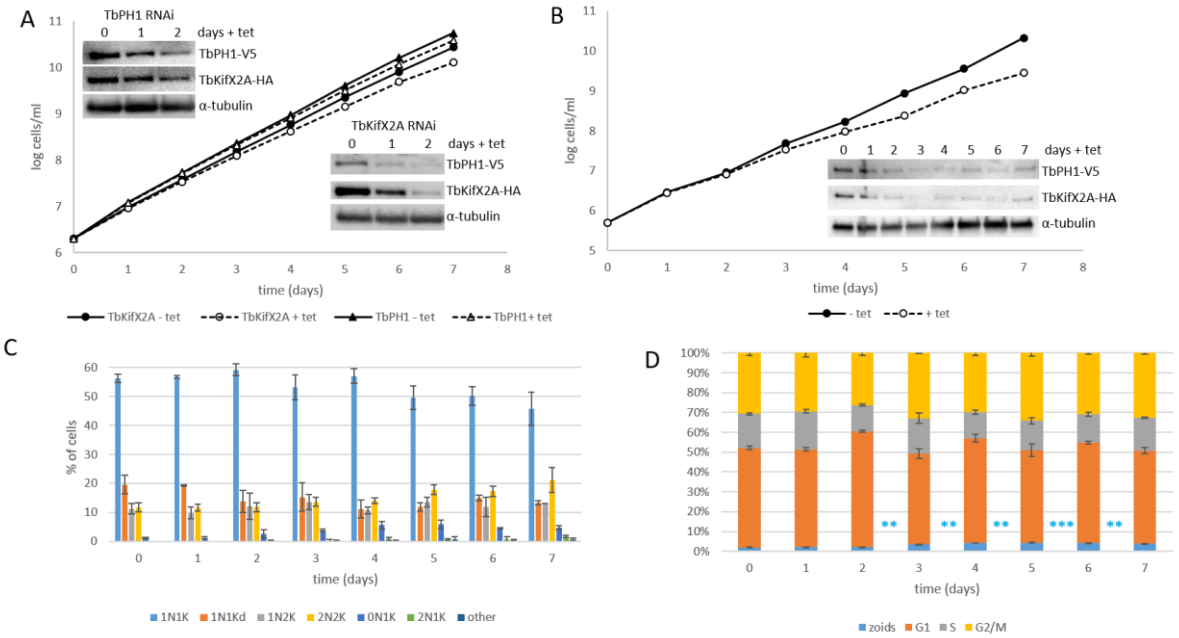
A
TbPH1 RNAi
0 1 2 days + tet
TbPH1-V5
TbKifX2A-HA
α-tubulin
TbKifX2A RNAi
0 1 2 days + tet
TbPH1-V5
TbKifX2A-HA
α-tubulin
log cells/ml
time (days)
TbKifX2A - tet
TbKifX2A + tet
TbPH1 - tet
TbPH1+ tet
B
0 1 2 3 4 5 6 7 days + tet
TbPH1-V5
TbKifX2A-HA
α-tubulin
log cells/ml
time (days)
- tet
+ tet
C
% of cells
time (days)
1N1K
1N1Kd
1N2K
2N2K
0N1K
2N1K
other
D
time (days)
zoids
G1
S
G2/M

Fig. 9

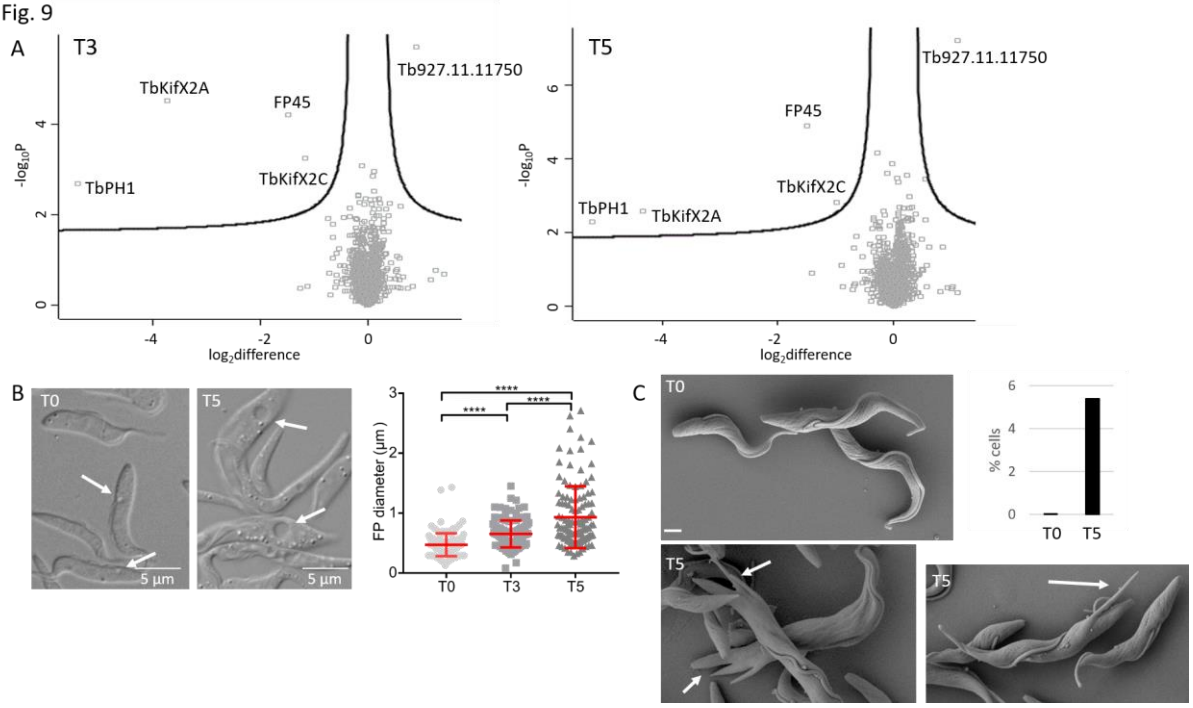
A
T3
TbKifX2A
FP45
Tb927.11.11750
TbPH1
TbKifX2C
-log10P
log2difference
T5
Tb927.11.11750
FP45
TbKifX2C
TbPH1
TbKifX2A
-log10P
log2difference
B
T0
T5
5 µm
5 µm
FP diameter (µm)
****
****
T0
T3
T5
C
T0
T5
T5
% cells
T0
T5

Suppl. Fig. 1

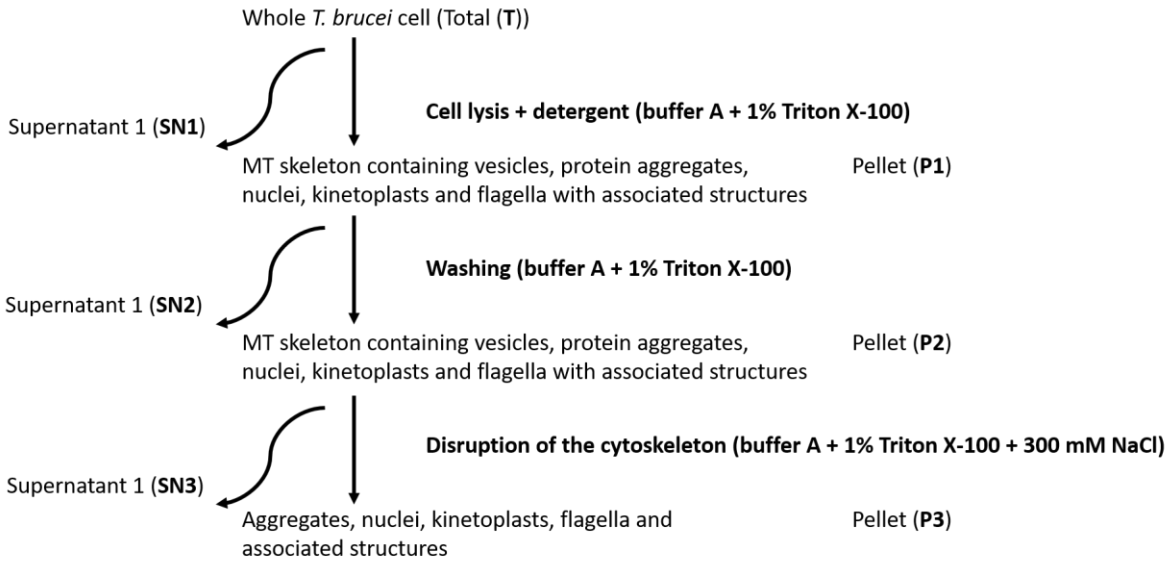
Whole *T. brucei* cell (Total (**T**))
Supernatant 1 (**SN1**)
Cell lysis + detergent (buffer A + 1% Triton X-100)
MT skeleton containing vesicles, protein aggregates, nuclei, kinetoplasts and flagella with associated structures
Pellet (**P1**)
Supernatant 1 (**SN2**)
Washing (buffer A + 1% Triton X-100)
MT skeleton containing vesicles, protein aggregates, nuclei, kinetoplasts and flagella with associated structures
Pellet (**P2**)
Supernatant 1 (**SN3**)
Disruption of the cytoskeleton (buffer A + 1% Triton X-100 + 300 mM NaCl)
Aggregates, nuclei, kinetoplasts, flagella and associated structures
Pellet (**P3**)

Suppl. Fig. 2

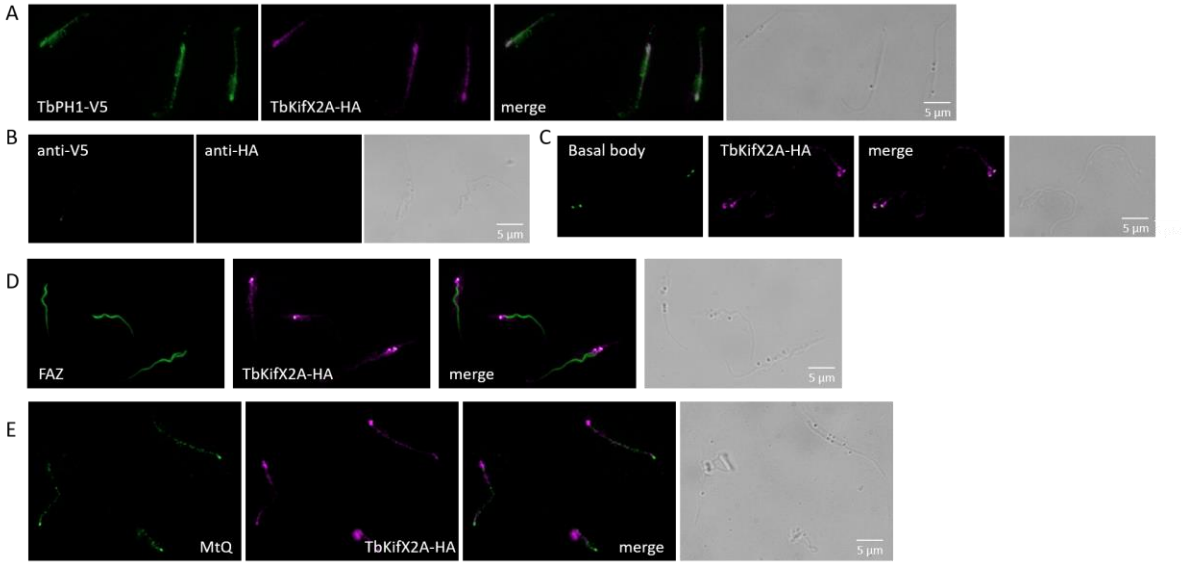
A
TbPH1-V5
TbKifX2A-HA
merge
5 µm
B
anti-V5
anti-HA
5 µm
C
Basal body
TbKifX2A-HA
merge
5 µm
D
FAZ
TbKifX2A-HA
merge
5 µm
E
MtQ
TbKifX2A-HA
merge
5 µm

Suppl. Fig. 3

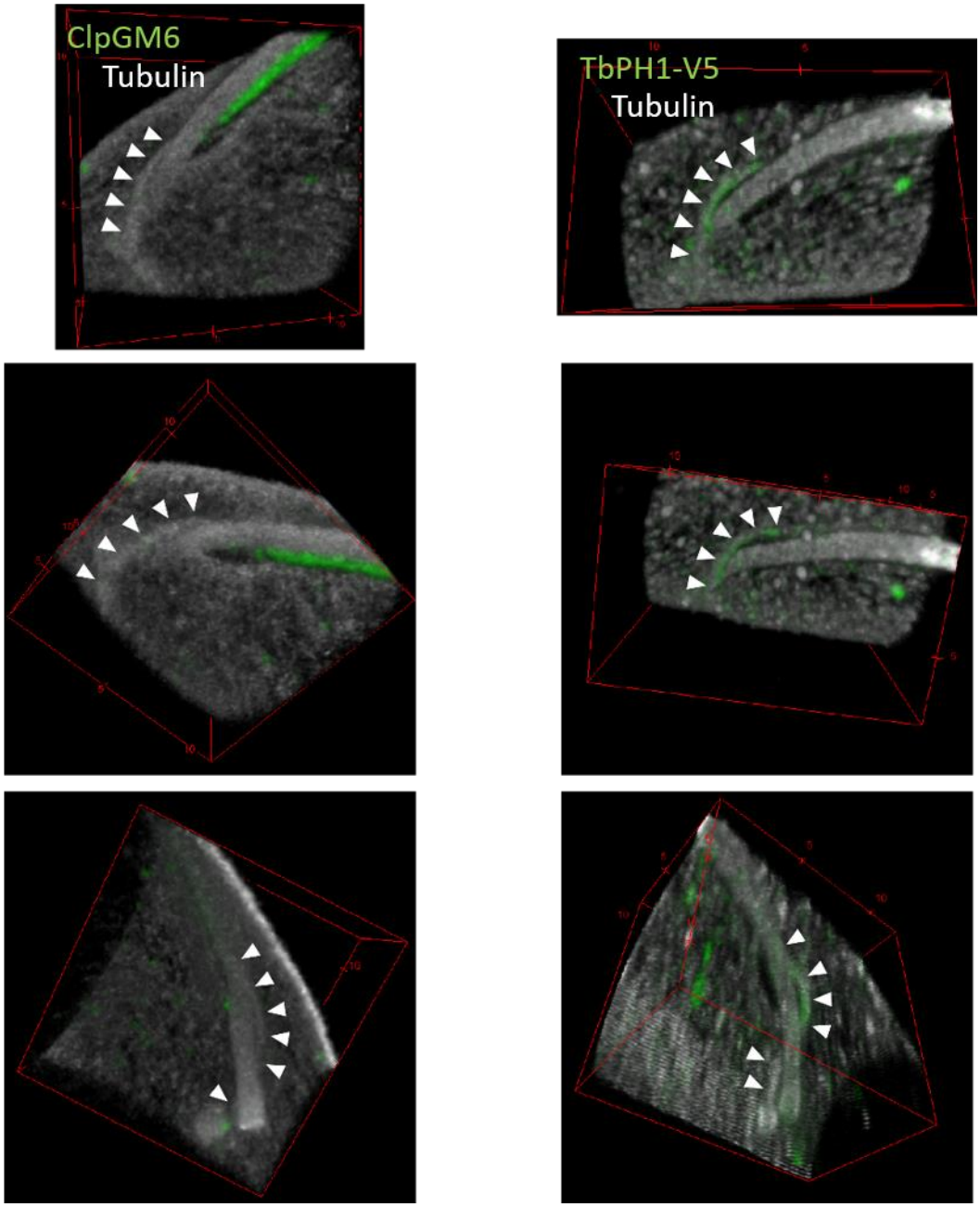

Suppl. Fig. 4

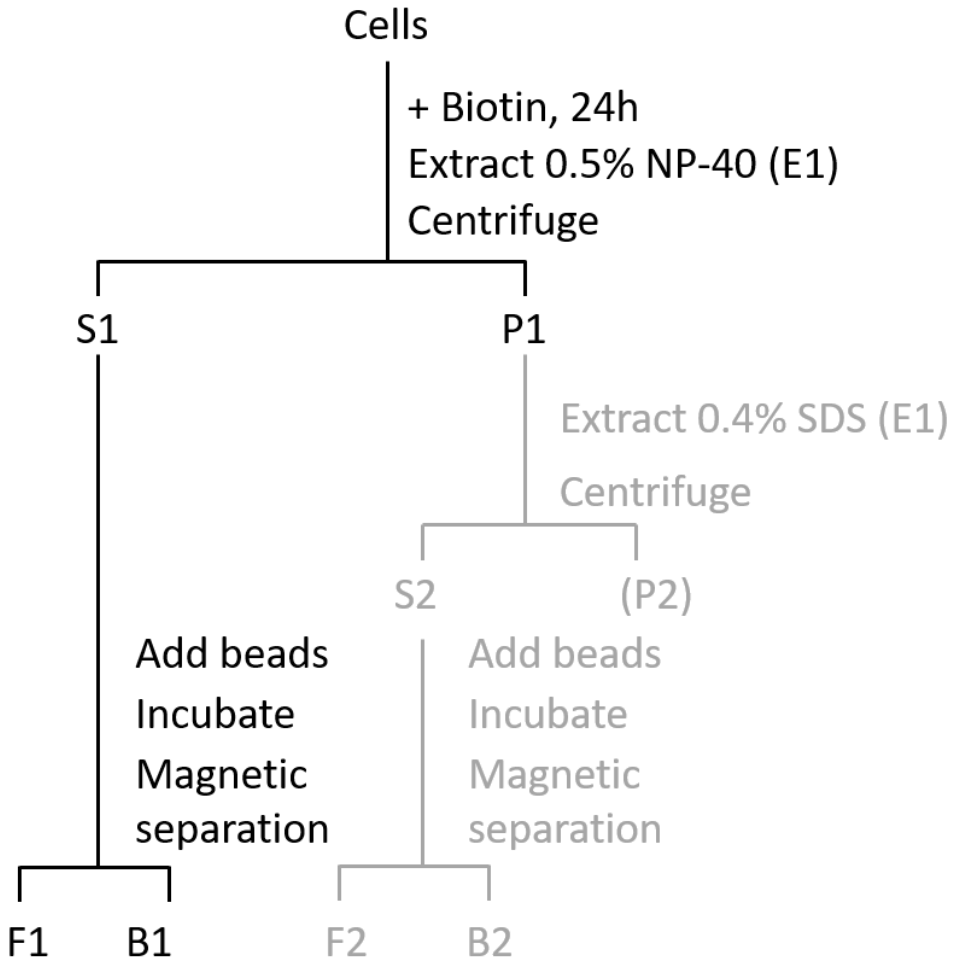
Cells
+ Biotin, 24h
Extract 0.5% NP-40 (E1)
Centrifuge
S1
P1
Extract 0.4% SDS (E1)
Centrifuge
S2
(P2)
Add beads
Incubate
Magnetic separation
Add beads
Incubate
Magnetic separation
F1
B1
F2
B2

Suppl. Fig. 5

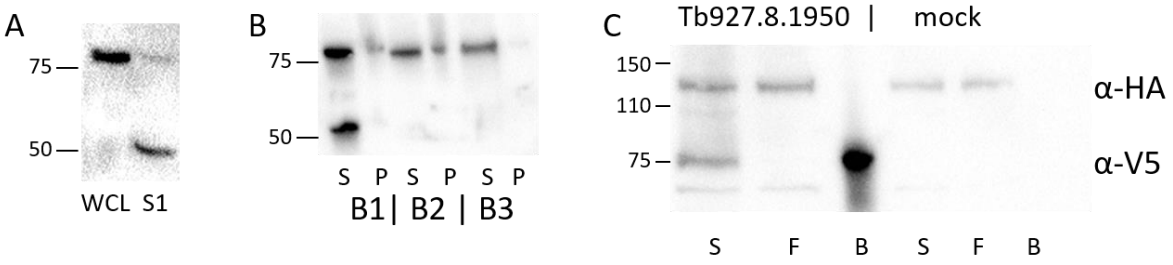
A
75
50
WCL S1
B
75
50
S P S P S P
B1| B2 | B3
C
Tb927.8.1950 | mock
150
110
75
α-HA
α-V5
S F B S F B

Suppl. Fig. 6

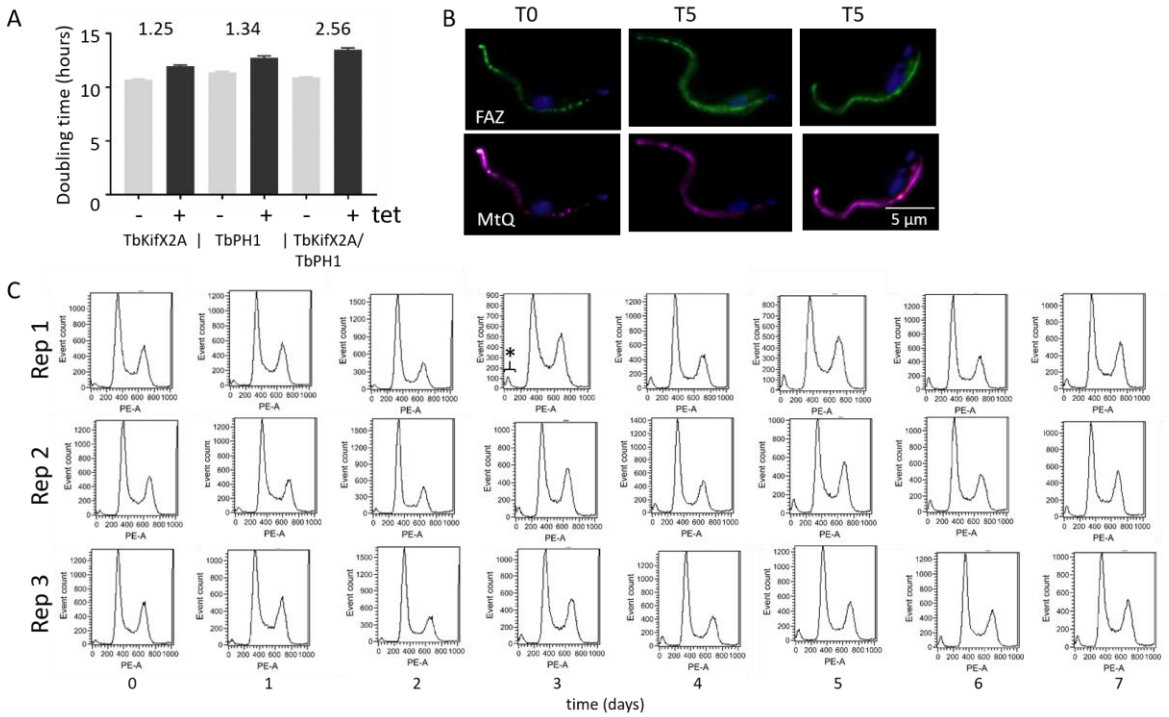
A
Doubling time (hours)
1.25
1.34
2.56
- + - + - + tet
TbKifX2A | TbPH1 | TbKifX2A/ TbPH1
B
T0
T5
T5
FAZ
MtQ
5 µm
C
Rep 1
Rep 2
Rep 3
Event count
PE-A
*
0
1
2
3
4
5
6
7
time (days)

Suppl. Fig. 7

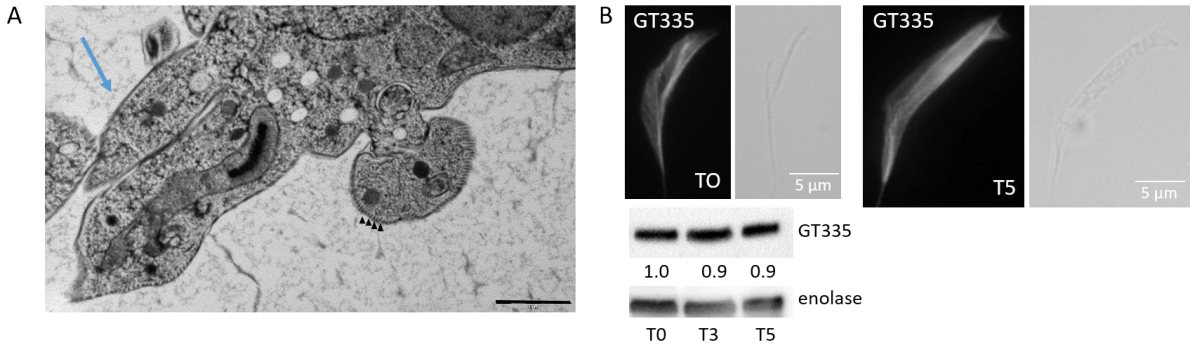

1442